Alma Mater Studiorum - Universita di Bologna

DOTTORATO DI RICERCA IN
Meccanica e Scienze Avanzate dell'Ingegneria
Ciclo XXVI
Settore Concorsuale di afferenza: 09/A2
Settore Scientifico disciplinare: ING-IND/13

DESIGN AND CHARACTERIZATION OF CURVED AND SPHERICAL FLEXURE HINGES FOR PLANAR AND SPATIAL COMPLIANT MECHANISMS

Presentata da:
Ing. Farid Parvari Rad

Coordinatore Dottorato:
Prof. Vincenzo Parenti Castelli

Relatori:
Prof. Vincenzo Parenti Castelli
Dott. Giovanni Berselli

Esame finale anno 2014

To my dear parents

and my lovely family

without whom I would never have been able to fulfill this dissertation.

Abstract

A flexure hinge is a flexible connector that can provide a limited rotational motion between two rigid parts by means of material deformation. These connectors can be used to substitute traditional kinematic pairs (like bearing couplings) in rigid-body mechanisms. When compared to their rigid-body counterpart, flexure hinges are characterized by reduced weight, absence of backlash and friction, part-count reduction, but restricted range of motion. There are several types of flexure hinges in the literature that have been studied and characterized for different applications. In our study, we have introduced new types of flexures with curved structures i.e. circularly curved-beam flexures and spherical flexures. These flexures have been utilized for both planar applications (e.g. articulated robotic fingers) and spatial applications (e.g. spherical compliant mechanisms). We have derived closed-form compliance equations for both circularly curved-beam flexures and spherical flexures. Each element of the spatial compliance matrix is analytically computed as a function of hinge dimensions and employed material. The theoretical model is then validated by comparing analytical data with the results obtained through Finite Element Analysis. A case study is also presented for each class of flexures, concerning the potential applications in the optimal design of planar and spatial compliant mechanisms. Each case study is followed by comparing the performance of these novel flexures with the performance of commonly used geometries in terms of principle compliance factors, parasitic motions and maximum stress demands. Furthermore, we have extended our study to the design and analysis of serial and parallel compliant mechanisms, where the proposed flexures have been employed to achieve spatial motions e.g. compliant spherical joints.

Contents

List of Abbreviations

MEMS   Micro Electromechanical Systems

FCM   Flexure-Based Compliant Mechanism

FEA   Finite Element Analysis

PRBM   Pseudo-Rigid-Body Model

SBF   Straight Beam Flexure

CCBF   Circularly Curved-Beam Flexure

SF   Spherical Flexure

List of Figures

List of Tables

Chapter 1

Introduction and Thesis Outline

> This chapter briefly introduces compliant mechanisms, their advantages and disadvantages in comparison with ordinary mechanisms and explains their contributions in different fields of mechanical and precision engineering. The motivation and outline of this thesis is further described.

1.1 Introduction to Compliant Mechanisms

A mechanism is a mechanical part or combination of parts that transforms input loads and motions into a desired set of output motions. A mechanism is commonly modeled as a set of interconnected rigid links by means of ideal rigid joints (kinematic pairs) which provide relative movements between the rigid links. Kinematic pairs ideally constrain the relative motion between rigid links i.e. constraining the pure rotational motion about a single point, or prismatic motion to a line, thus prevent any undesired motion produced from deflections and elastic deformations. When the flexibility and elastic deformations are used to provide desired relative motions, we meet a new class of mechanisms called compliant mechanisms. Compliant mechanisms gain their mobility by transforming an input force or energy into an output motion, undergoing an elastic deformation, due to the existence of flexible members in these mechanisms. The concept of using compliant members dates back to the late Paleolithic (about 35000 to 8000 B.C.) [1] when archery seems to have been invented by the late stone-age humans for war and hunting purposes (Fig. 1.1). Pulling the arrow, strain energy is stored in the arc and by releasing the arc, it is transformed to kinetic energy of the arrow creating the output motion. Strain energy is the same as elastic potential energy that is stored in a spring. This concept has been extended to use in more heavier weapons later, i.e. catapults that first used by Syracusean Greeks in 399 B.C. [2]. Catapults were the artillery of the
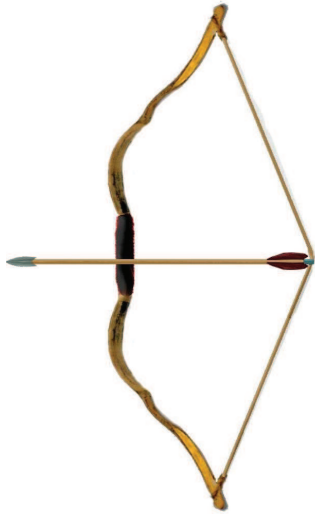
Figure 1.1: The bow and arrow

Figure 1.2: Greek palintone: A
torsion-powered catapult

ancient armies to hurl heavy objects or arrows over a large distance in early battles for winning the war. A Greek "Palintone" type ballista catapult is shown in Fig. 1.2. It was capable of throwing a three pound concrete ball more than 200 yards [3]. Palintone is called a torsion-powered catapult since strain energy is provided by using tightly string coils of rope like a torsional spring.

The use of compliant members were limited mostly for war machines until the last century. Recently, compliant mechanisms become important components for various applications in different research areas such as micro-electromechanical systems (MEMS), robotics, precision engineering, biomechanics, etc. They are also used frequently in our daily life. Some of the most commonly used compliant mechanisms are shown in Fig. 1.3.

1.2   Advantages

Compliant mechanisms encompass several advantages in comparison with kinematic pairs that make them suitable for a wide range of applications. These advantages can be classified as follows [4]:

- **Single Layer Fabrication:** Compliant mechanisms can be made from a single layer of material. This makes them compatible with different fabrication methods available for MEMS, such as surface micromachining, bulk micromachining and the LIGA (Lithographie or lithography/Galvanoformung or electroforming/Abformung or molding) process using a compact synchrotron radiation (SR) source [5].

Figure 1.3: Commonly used compliant devices: Binder clips, paper clips, hair clips, backpack latch, eyelash curlers and nail clippers

- **No Need for Assembly:** Fully compliant mechanisms that gain all of their motion from the deflection of flexible members are usually fabricated in a single piece and do not require assembly of different components.

- **Compactness:** Some compliant mechanisms can be manufactured in a compact form, making them ideal for micro-scale and precision engineering applications.

- **No Friction Losses:** Considering the fact that compliant mechanisms gain their motion from deflection of flexible members rather than rigid body joints, the friction relevant to rubbing surfaces can be removed. This eliminates the need for lubrication and reduces wear.

- **Absence of Wear:** Wear is the erosion caused by physical interactions between contacting surfaces and occurs in kinematic pairs. It can be particularly problematic for small range applications in biomechanics and precision mechanisms. Wear can be removed by eliminating friction between contacting surfaces. This will increase the life cycles of mechanical systems.

- **No Need for Lubrication:** Absence of friction losses in compliant mechanisms, eliminates the need for lubrication. This could have a significant role in applications that suffer an easy lubri-

cation process.

- **High Accuracy:** The absence of friction and wear, as described above, along with the backlash-free motion inherent in compliant mechanisms, increase their precision and make them preferable to use in high accuracy instruments.

- **High Reliability:** The aforementioned characteristics of compliant mechanisms, their light weight and reduced maintenance result in high reliability.

1.3 Challenges

Despite all the advantages that compliant mechanisms comprise in comparison with ordinary mechanisms, they also have some challenges:

- **Limited Range of Motion:** Since the relative motion between rigid parts is provided by means of material deformation, compliant mechanisms are unable to undergo continuous motions and are capable of providing limited range of motion.

- **Parasitic Motions:** The relative motion provided by compliant mechanisms is not a pure motion and there are always secondary undesired motions produced by the complex deformation behavior of these mechanisms. The secondary undesired motions are called parasitic motions.

- **Nonlinear Motions:** Some compliant mechanisms require to undergo large deformations where linearized beam equations are no longer valid. Nonlinear equations that account for the geometric nonlinearities caused by large deflections must be used. This can make their design and analysis more complicated.

- **Fatigue Failures:** Most compliant mechanisms need to undergo repeated loading and to operate under cyclic stress conditions which make them vulnerable to fatigue failures.

1.4 Motivation

As previously described, compliant mechanisms gain their mobility from the deflection of flexible members. These flexible members are called flexure hinges. A flexure hinge, is a flexible and slender region between two rigid parts that can provide a relative rotation between the rigid parts by means of material deformation. They can be usually obtained by machining a blank piece of material, thus obtaining the so-called Flexure-Based Compliant Mechanisms (FCMs) in which compliance is concentrated within the relatively small regions of the flexures. FCMs are
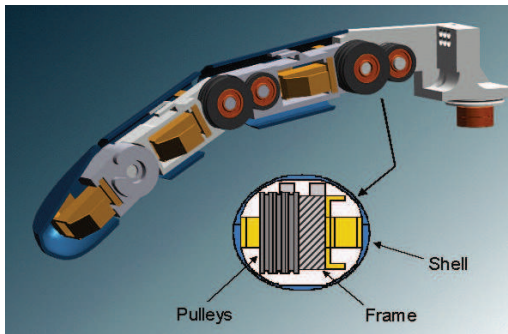
Figure 1.4: Pulley-based articulated robotic finger [6]
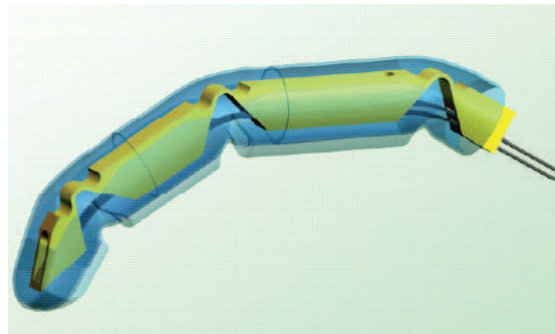
Figure 1.5: FCM-based articulated robotic finger [6]

widely used in different research areas considering their wide advantages over traditional rigid-body mechanisms. Some examples of implementing FCMs in different fields are translation micro-positioning stages, piezoelectric actuators and motors, high-accuracy alignment devices for optical fibers, missile-control devices, displacement and force amplifiers/deamplifiers, orthotic prostheses, antennas, valves, scanning tunneling microscopes, accelerometers, gyroscopes, high-precision cameras, nano-lithography, robotic micro-displacement mechanisms, nano-scale bioengineering, small-scale insect-like walking robots, actuation devices for unmanned micro aerial vehicles, or nano-imprint technology.

The main focus of this study is on designing and developing FCMs for possible applications particularly in areas as mechanical and precision engineering, robotics, and biomedical engineering. For instance, Fig. 1.4 shows an articulated robotic finger for applications in anthropomorphic robotic hands. Anthropomorphic robotic hands have been widely studied because of their inherent similarity to the human hand and their contribution in various fields ranges from hand prosthetics to healthcare robots and robotic surgeries to space explorations. However, it has been always difficult to mimic the human hand due to its unique biological features and kinematic behavior. Thus, robotic hands often require complicated joint mechanism such as hinges, linkages, pulleys, belts and sensors to be designed and developed in a small space in order to achieve the complex behavior of the human hand.

From a design perspective, the introduction of FCMs in serial articulated chains, like anthropomorphic hands and prosthesis, seems promising as it can allow the generation of very slender and light mechanisms that better reproduce biological structures with a reduced number of parts, easy to be manufactured and assembled, cheap and compatible with the required features. The example of such an articulated robotic finger is shown in Fig. 1.5.

1.5   Contribution

The main contribution of this thesis is to design and characterize new types of flexure hinges with curved centroidal axes for both planar and spatial applications. First, Circularly Curved-Beam Flexures (CCBFs) will be characterized and particularly designed for planar applications such as articulated robotic fingers. The spatial compliance of these flexures will be evaluated and their closed-form compliance equations will be derived. Spherical Flexures (SFs) will be then introduced and specifically designed for spatial applications. These flexures will be evaluated concerning their capabilities in generating spherical motions and they will be used in compliant spherical chains (in particular, for the design of a new compliant spherical joint). Further evaluations will be carried out to compare the main characteristics of the aforementioned flexures with commonly used flexure hinges.

1.6   Thesis outline

- Chapter 1 briefly introduces compliant mechanisms, their advantages and disadvantages in comparison with ordinary mechanisms and explains their contributions in different fields of mechanical and precision engineering. The motivation and outline of this thesis is further described in this chapter.

- Chapter 2 is dedicated to a brief presentation of flexure hinges which are the main components of flexure-based compliant mechanisms. Flexure hinges provide the relative motion between the adjoining rigid parts by means of elastic deformation. The common methods used for designing and analyzing flexure hinges accompanied by their literature review are described in this chapter.

- In Chapter 3, the closed-form compliance equations for circularly curved-beam flexures are derived. Following a general modeling procedure, each element of the spatial compliance matrix is analytically computed as a function of both hinge dimensions and employed material. The theoretical model is then validated by comparing analytical data with the results obtained through finite element analysis. Finally, a case study is presented concerning the potential application of these types of flexures in the optimal design of compliant robotic fingers.

- In Chapter 4, the closed-form compliance equations for spherical flexures are derived. Each element of the spatial compliance matrix is analytically computed as a function of both hinge dimensions and employed material. The theoretical model is then validated by relating analytical data with the results obtained through finite element analysis. Finally, for a generic loading condition, spherical flexures are compared to circularly curved-beam flexures in terms of secondary compliance factors and maximum stress.

- Chapter 5 introduces and investigates a fully compliant spherical chain that is obtained by the in-series connection of two identical primitive spherical flexures with coincident center of spherical

motion. The compliance matrix of the proposed chain is obtained via an analytical procedure and validated via finite element analysis. Comparison with an equivalent fully compliant chain employing straight beam flexures is also provided to highlight the added benefits when using primitive spherical flexures.

- Chapter 6 represents a new type of passive compliant spherical joint. The joint is made by the in-parallel connection of two fully compliant spherical chains. Each chain is composed of three identical spherical flexures connected in-series with mutually orthogonal axes. The closed-form compliance equations for the spherical joint are derived via the previously described analytical method. The compliant spherical chain is also evaluated comparing with the equivalent compliant serial chain employing straight beam flexures.

- Chapter 7 summarizes the main contributions of this thesis.

Chapter 2

Background and Literature

This chapter is dedicated to a brief presentation of flexure hinges which are the main components of flexure-based compliant mechanisms. Flexure hinges provide the relative motion between the adjoining rigid parts by means of elastic deformation. The common methods used for designing and analyzing flexure hinges accompanied by their literature review are described in this chapter.

2.1 Flexure Hinges

A flexure hinge is a slender flexible connector that provides the relative rotational motion between two adjacent rigid members via material deformation rather than by the sliding or rolling of mating surfaces (Fig. 2.1). The flexure hinge is also called as "flexural pivot" or simply "flexure". When compared to their rigid-body counterparts, flexure hinges are characterized by reduced weight, absence of backlash and friction, one-piece manufacturing with no need of assembling (i.e. reduced production costs), but restricted range of motion.

Flexure hinges can be classified as single-axis, two-axis and multi-axis flexures [7]. Single-axis flexure hinges are supposed to be compliant with respect to one single axis (compliant or sensitive axis) and stiff as much as possible about all other axes. Single-axis flexures are designed for two-dimensional applications that have a planar motion and they can be fabricated by removing material from a blank piece using manufacturing processes such as end-milling, electrodischarge machining (EDM), laser cutting, metal stamping, or photolithographic techniques for MEMS. Two- and multi-axis flexure hinges possess two or more compliant axes and are suitable for three-dimensional applications with spatial motions. They can be usually machined by lathe-turning or precision casting.
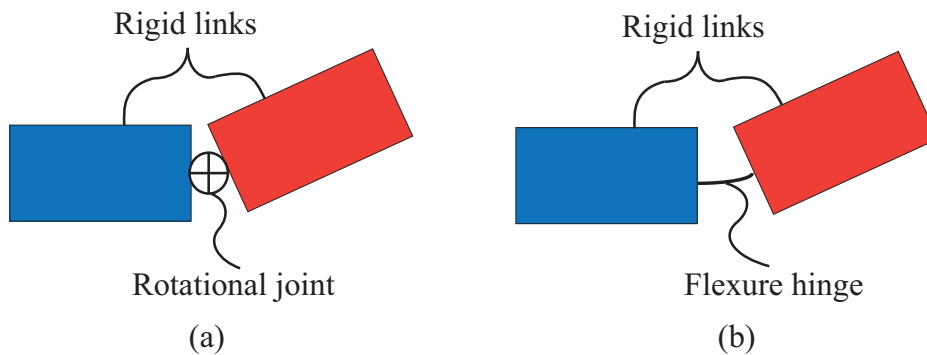
Figure 2.1: (a) Conventional rigid-body joint (b) Flexure hinge

Although flexure hinges provide monolithic connections with no backlash and hysteresis, they usually bring the following disadvantages: limited range of motion, parasitic motions and stress concentrations. For this reason, to be effective, flexure hinges need to be conceived and optimized for the specific application at hand. However it is not always straight forward to study and analyze flexure hinges to achieve design demands for different applications. Analytical methods provide accurate and precise means of evaluating and designing flexure hinges but they can be complicated when flexures infold complex geometrical shapes or deforming out of linearized beam theory approximation. Finite Element Analysis (FEA) and simplified analytical methods such as Pseudo-Rigid-Body Model (PRBM) are also efficient tools that can be utilized to tackle such difficulties. In the following of this chapter, the available techniques on designing and characterizing flexure hinges, are briefly reviewed.

2.2 Pseudo-Rigid-Body Model

The PRBM is a tool that connects rigid-body mechanism theory to compliant mechanism theory and provides the possibility of using traditional rigid-body modeling methods in the design and analysis of compliant mechanisms. The PRBM principally treats flexures as rigid links connected at appropriately placed pins, with torsional springs to represent the compliance behavior of flexible members that undergo large and nonlinear deflections. Several works have been dedicated to study and develop the PRBM for applications both in macro-scale range([4], [8], [9], [10], [11], [12] and etc.) and MEMS([13], [14], [15], [16] and etc.).

Let us consider a small-length flexural pivot [9] shown in Fig. 2.2. When the length of the flexural pivot (l) is much smaller than the length of the rigid part (L), and the flexural pivot is much less stiffer than the rigid part, the motion of the system can be modeled by a pin joint connecting two
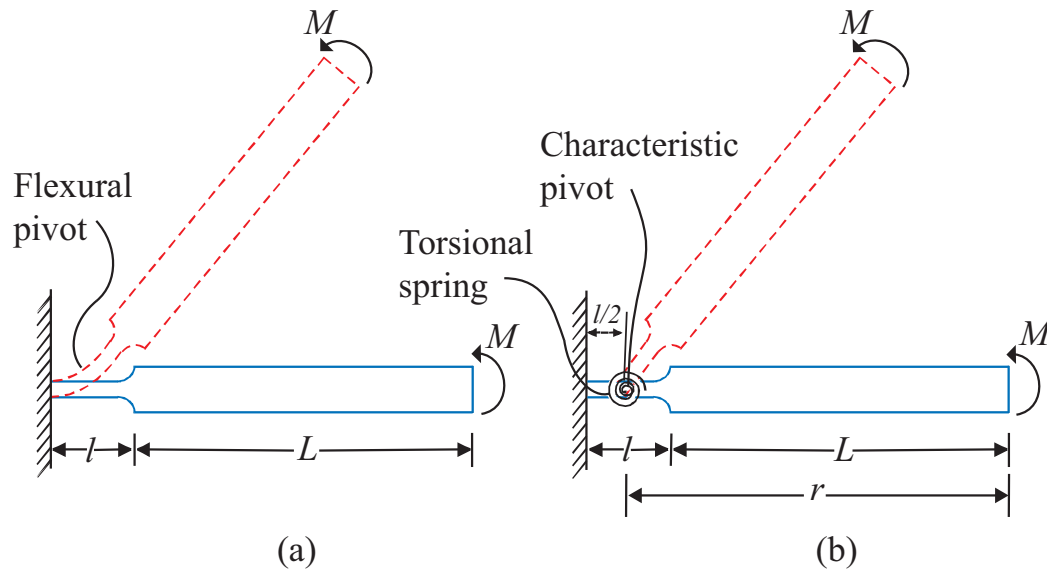
Figure 2.2: (a) A small-length flexural pivot (b) Its pseudo-rigid-body model

rigid links, called as "the characteristic pivot". The characteristic pivot is located at the center of the flexural pivot and the length of the pseudo-rigid link, r, is defined as follows:

$$r = L + \frac{l}{2} \tag{2.1}$$

The elastic deformation of the flexural pivot is modeled by a torsional spring with the spring constant K:

$$K = \frac{EI}{l} \tag{2.2}$$

where E, is the material Young's modulus and I is the second moment of area.

The PRBM can be extended to other segments such as fixed-guided flexible segments, pinned-pinned segments, beams loaded with a moment at the end, and beams with follower loads. Complete details for pseudo-rigid-body modeling of different types of segments can be found in [4].

2.3 Compliance-Based Design of Flexure Hinges

In spite of the fact that the PRBM is an exclusive tool in modeling and designing FCMs, it can suffer from some limitations. First, torsional springs are incapable of modeling axial and lateral deformations resulting from axial and transversal forces that usually exist in loading flexure hinges. Second, there are several FCMs that are intended to operate in small-displacement range, producing small levels of output motion within acceptable levels of stress, where large-displacement theory does not apply. Compliance-based design of flexure hinges can overcome such difficulties.
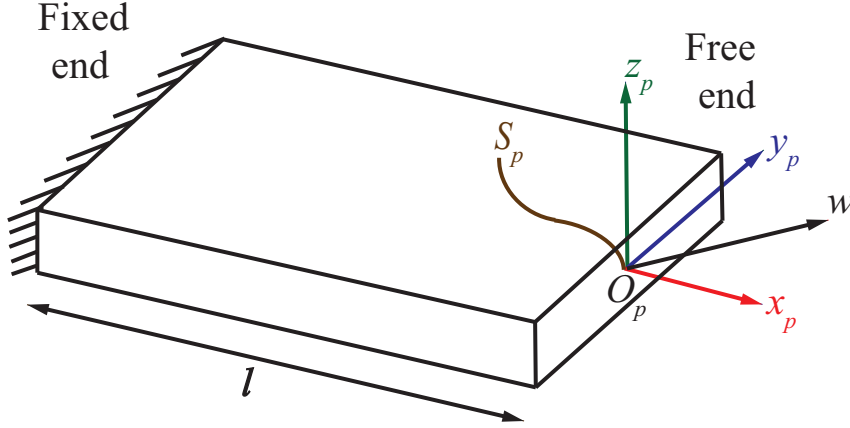
Figure 2.3: Straight beam flexure loaded at the free end

In this approach, a flexure hinge is treated as a complex spring element with full degrees of freedom in response to quasi-static loading. Closed-form compliance equations for flexure hinges are derived via analytical or finite element methods to design and characterize flexure hinges in terms of its geometrical parameters and the employed material. Within the validity limits of the superposition principle (which assumes linear elastic materials and small deflections), the kineto-static behavior of a flexural hinge in the 3D space can be deduced by the analysis of its compliance matrix [17]. For instance, let us consider a Straight Beam Flexure (SBF) with length l that is generically loaded at the free end (Fig. 2.3). Given an external perturbation wrench, ${}^P\mathbf{w}$, acting on the flexure free end whose components are expressed with respect to the beam free end coordinate frame S_p (with axes x_p, y_p, z_p), the incremental displacement vector, ${}^P\mathbf{s}$, can be expressed as:

$$
{}^P\mathbf{s} = \begin{bmatrix} {}^P\mathbf{u} \\ \hline {}^P\boldsymbol{\theta} \end{bmatrix} = {}^P\mathbf{C} \cdot \begin{bmatrix} {}^P\mathbf{f} \\ \hline {}^P\mathbf{m} \end{bmatrix} = {}^P\mathbf{C} \cdot {}^P\mathbf{w} \tag{2.3}
$$

where ${}^P\mathbf{s}$ is composed of an incremental translation ${}^P\mathbf{u} = \begin{bmatrix} u & v & w \end{bmatrix}^T$ and an incremental rotation ${}^P\boldsymbol{\theta} = \begin{bmatrix} \alpha & \phi & \psi \end{bmatrix}^T$, whereas ${}^P\mathbf{w}$ is composed of a force vector ${}^P\mathbf{f} = \begin{bmatrix} f_x & f_y & f_z \end{bmatrix}^T$ and a torque vector ${}^P\mathbf{m} = \begin{bmatrix} m_x & m_y & m_z \end{bmatrix}^T$. As a consequence, the compliance matrix ${}^P\mathbf{C}$ is a 6x6 matrix with frame-dependent entries of non homogenous physical dimensions, which relates the external wrench to the resulting translations and rotations and it can be expresses as follows [18]:

$$
{}^{P}\mathbf{C} =
\begin{bmatrix}
\frac{l}{EA} & 0 & 0 & 0 & 0 & 0 \\
0 & \frac{l^3}{3EI_y} & 0 & 0 & 0 & \frac{l^2}{2EI_y} \\
0 & 0 & \frac{l^3}{3EI_x} & 0 & -\frac{l^2}{2EI_x} & 0 \\
0 & 0 & 0 & \frac{l}{GJ} & 0 & 0 \\
0 & 0 & -\frac{l^2}{2EI_x} & 0 & \frac{l}{EI_x} & 0 \\
0 & \frac{l^2}{2EI_y} & 0 & 0 & 0 & \frac{l}{EI_y}
\end{bmatrix}
\tag{2.4}
$$

where A, I_x, I_y, J, E and G are respectively cross section area, principal and polar moments of inertia of the beams cross section, Youngs modulus and shear modulus of the employed material. In this scenario, the knowledge of the hinge compliance behavior, even in the small displacement range, can be extremely useful both for comparison purposes and for first-attempt sizing the hinge dimensions. Closed-form compliance equations provide useful means to evaluate flexure hinges on different basis i.e. principle compliance factors, sensitivity to undesired or parasitic motions and maximum stress levels. Several studies have been proposed to design and characterize flexure hinges on this basis. For instance, Paros and Weisbord [19] represented circular flexure hinges (Fig. 2.4(a)) and provided compliance equations for them. Zettl et al. [20] performed FEA to model right-circular flexure hinges. Xu and King [21] used this technique for investigating the performance of elliptical (Fig. 2.4(b)) and corner-filleted flexure hinges (Fig. 2.4(c)). Lobontiu et al. [22] represented the equations for corner-filleted flexure hinges using the Castigliano's second theorem. Schotborgh et al. [23] applied FEA to present dimensionless design graphs for three typical circular, corner-filleted and cross flexure hinges (Fig. 2.4(d)) in order to provide a reasonable comparison between them for design purposes. Tian et al [24] used numerical methods for dimensionless graph analysis of three filleted V-shaped (Fig. 2.4(e)), cycloidal (Fig. 2.4(f)) and circular flexure hinges. Chen et al. [25] obtained analytical equations for elliptical-arc-fillet flexure hinges. In this thesis, we have introduced new types of flexure hinges with curved axes i.e. CCBFs (Fig. 2.4(g)) and SFs (Fig. 2.4(h)) for both planar applications like articulated robotic fingers and spatial applications such as compliant spherical mechanisms. All the closed-form compliance equations for these flexures are derived and represented as a function of the hinge geometric parameters and employed material. Further analysis have been carried out to evaluate the performance of the proposed flexures with commonly used ones such as SBFs.
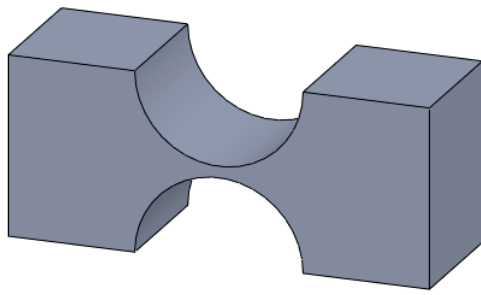
(a) Circular flexures
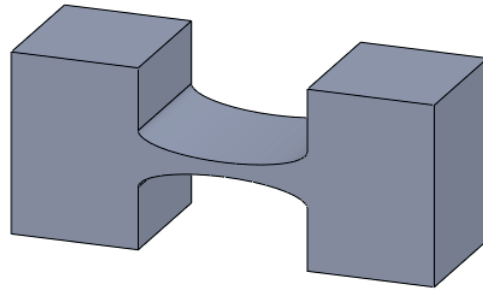
(b) Elliptical flexures
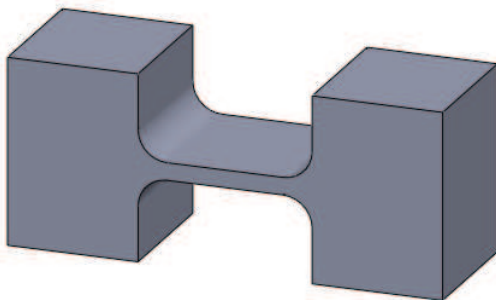
(c) Corner-filleted flexures
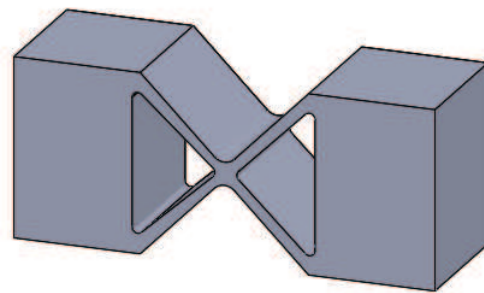
(d) Cross flexures
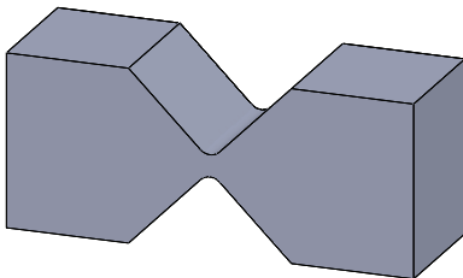
(e) Filleted V-shaped flexures
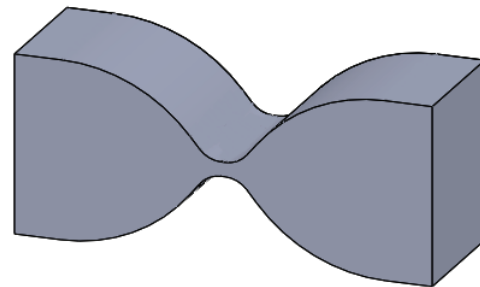
(f) Cycloidal flexures
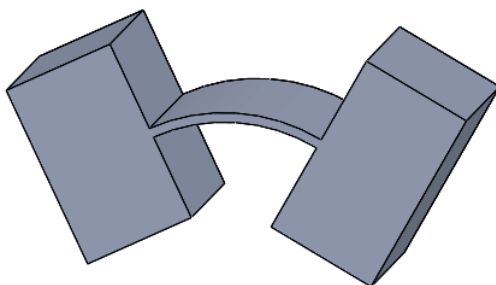
(g) Circularly curved-beam flexures
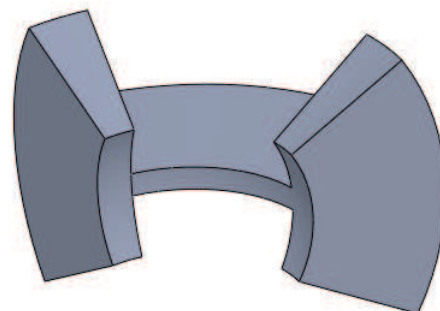
(h) Spherical flexures

Figure 2.4: Different types of flexures

Chapter 3

Design and Characterization of Circularly Curved-Beam Flexure Hinges for Planar Compliant Mechanisms

In this chapter, the closed-form compliance equations for circularly curved-beam flexures are derived. Following a general modeling procedure, each element of the spatial compliance matrix is analytically computed as a function of both hinge dimensions and employed material. The theoretical model is then validated by comparing analytical data with the results obtained through finite element analysis. Finally, a case study is presented concerning the potential application of these types of flexures in the optimal design of compliant robotic fingers.

3.1   Introduction

As described earlier, flexure hinges have found a wide range of applications in different fields such as serial articulated chains, like anthropomorphic hands and prosthesis. For instance, Fig. 3.1 and Fig. 3.2 depict two compliant robotic fingers, previously proposed by Lotti and Vassura [26], that employ either SBFs or CCBFs as possible substitutes for traditional revolute joints (the corresponding hinge rotation being defined as principal rotation [27]). In this case, regardless of the flexure topology, the use of flexible joints allows one-piece manufacturing and enhanced performance in terms of robustness and safety when interacting with unknown environments or

Figure 3.1: Mono-piece robotic finger
employing SBFs [26]
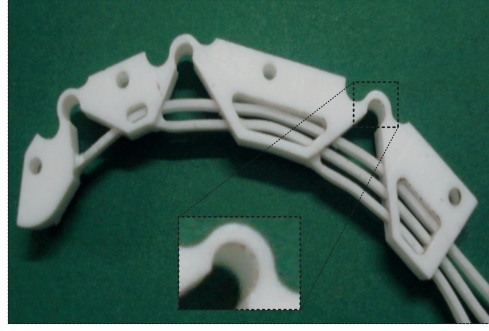
Figure 3.2: Mono-piece robotic finger
employing CCBFs [26]

humans (e.g. [28]). In this chapter, the general approach for deriving compliance equations of cantilever curved beams is first described and the closed-form compliance equations for CCBFs are obtained. CCBFs are then evaluated and compared with SBFs in terms of selective compliance and maximum achievable principal rotation for possible applications like robotic fingers as depicted in Fig. 3.1 and Fig. 3.2.

The relevant contribution of this chapter is published in [29] and [30].

3.2 General Approach for Deriving Compliance Equations of Cantilever Curved Beams

The direct analytical method proposed in [31] is used for explicitly deriving the closed-form compliance equations of cantilever curved beams. With reference to Fig. 3.3, let consider a cantilever curved beam with a uniform cross section and generically loaded at the free end. Node 1 and node 2 are located on the beam fixed and free end respectively. Let the external load, $^g\mathbf{w}$, and the corresponding deformation, $^g\mathbf{s}$ be expressed with respect to a predefined global coordinate system S_g.

Then, a local coordinate system S_l centered on the centroid of a generic beam cross section can be defined. In particular, this local coordinates are denoted by $\mathbf{l}$, $\mathbf{m}$ and $\mathbf{n}$, namely the tangent vector and the principal vectors of the cross section. The relation between local and global coordinates can be written as follows:

$$\begin{bmatrix} \mathbf{l} \\ \mathbf{m} \\ \mathbf{n} \end{bmatrix} = \begin{bmatrix} l_x(s) & l_y(s) & l_z(s) \\ m_x(s) & m_y(s) & m_z(s) \\ n_x(s) & n_y(s) & n_z(s) \end{bmatrix} \cdot \begin{bmatrix} \mathbf{i} \\ \mathbf{j} \\ \mathbf{k} \end{bmatrix} = {}^l\mathbf{R}_g(s) \cdot \begin{bmatrix} \mathbf{i} \\ \mathbf{j} \\ \mathbf{k} \end{bmatrix} \qquad (3.1)$$

where s refers to the coordinate variable along the curve and $^l\mathbf{R}_g(s)$ is the rotation matrix that relates global and local coordinate frames. Omitting for clarity the superfix g or l in the vector elements, the curve defining the centroid of the beam cross sections, curve C, in the global
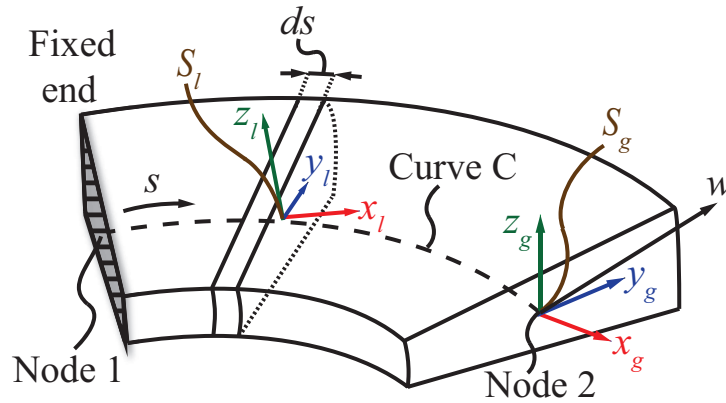
Figure 3.3: Cantilever curved beam loaded at the free end

coordinates can be expressed by:

$$^g\mathbf{r}(\mathbf{s}) = x(s)\mathbf{i} + y(s)\mathbf{j} + z(s)\mathbf{k} \tag{3.2}$$

The load $^g\mathbf{w}$ acting on the free end is balanced by a load $^l\mathbf{w}'$ acting on element ds of the curve C. This load $^l\mathbf{w}'$ produces a deformation per unit length, $\mathbf{E}$, on the same element. The vectors $^l\mathbf{w}'$ and $^l\mathbf{E}$ and the corresponding analytical relation can be expressed as:

$$^l\mathbf{w}' = \begin{bmatrix} f_l & f_m & f_n & m_l & m_m & m_n \end{bmatrix}^T \tag{3.3}$$

$$^l\mathbf{E} = \begin{bmatrix} \varepsilon_{ll} & \gamma_{lm} & \gamma_{ln} & \kappa_{ll} & \kappa_{lm} & \kappa_{ln} \end{bmatrix}^T$$

$$^l\mathbf{w}' = \mathbf{K} \cdot {}^l\mathbf{E}$$

The matrix $\mathbf{K}$ is the stiffness matrix of the element ds that can be written as:

$$\mathbf{K} = \begin{bmatrix} EA & 0 & 0 & 0 & 0 & 0 \\ 0 & b_m GA & 0 & 0 & 0 & 0 \\ 0 & 0 & b_n GA & 0 & 0 & 0 \\ 0 & 0 & 0 & GJ & 0 & 0 \\ 0 & 0 & 0 & 0 & EI_m & 0 \\ 0 & 0 & 0 & 0 & 0 & EI_n \end{bmatrix} \tag{3.4}$$

where A, b_m, b_n, I_m, I_n, J, E and G are, respectively, cross section area, shear coefficients, principal moments of inertia and polar moment of inertia of the beam's cross section, Young's modulus and shear modulus of the employed material. The deformation, $d^l\mathbf{s}'$, of the element ds, due to the load $^l\mathbf{w}'$, is defined by:

$$d^l\mathbf{s}' = \begin{bmatrix} du' & dv' & dw' & d\alpha' & d\phi' & d\psi' \end{bmatrix}^T = \mathbf{E} \cdot ds \tag{3.5}$$

where u', v', w' and α', ϕ', ψ' are respectively displacements and rotations of the element ds in the $\mathbf{l}$, $\mathbf{m}$ and $\mathbf{n}$ directions. The load $^{l}\mathbf{w}'$, acting on ds due to the presence of the load $^{g}\mathbf{w}$ on the free end, can be computed via the adjoint transformation matrix $^{l}\mathbf{T}_{g}$ between the global and local coordinates. In particular, The following relation holds:

$$^{l}\mathbf{w}' = {}^{l}\mathbf{T}_{g} \cdot {}^{g}\mathbf{w} \tag{3.6}$$

The adjoint matrix $^{l}\mathbf{T}_{g}$ is a function of the curvilinear coordinate s and can be computed from Eq. 3.1 and Eq. 3.2:

$$^{g}\mathbf{T}_{l}(s) = \left[\begin{array}{c:c} {}^{g}\mathbf{R}_{l}(s) & \mathbf{0} \\ \hdashline {}^{g}\mathbf{R}_{l}(s) \cdot {}^{g}\widetilde{\mathbf{r}}(s) & {}^{g}\mathbf{R}_{l}(s) \end{array} \right] \tag{3.7}$$

where $^{g}\mathbf{r_{s}} = {}^{g}\mathbf{r_{2}} - {}^{g}\mathbf{r}$ is the position vector connecting the centroid of the section to node 2. In addition, the deformation of the element ds, $d^{l}\mathbf{s}'$, causes a deformation at the free end, $d^{g}\mathbf{s}$, that can be calculated using the following equation:

$$d^{g}\mathbf{s} = {}^{l}\mathbf{T}_{g}^{T} \cdot d^{l}\mathbf{s}' \tag{3.8}$$

By merging Eqs. 3.3, 3.5, 3.6 and 3.8 one can obtain:

$$d^{g}\mathbf{s} = {}^{l}\mathbf{T}_{g}^{T} \cdot \mathbf{K}^{-1} \cdot {}^{l}\mathbf{T}_{g} \cdot {}^{g}\mathbf{w} \cdot ds \tag{3.9}$$

By integrating Eq. 3.9, the relation between the load $^{g}\mathbf{w}$ and the deformation $^{g}\mathbf{s}$ of the free node becomes as follows:

$$^{g}\mathbf{s} = {}^{g}\mathbf{C} \cdot {}^{g}\mathbf{w} \tag{3.10}$$

where:

$$^{g}\mathbf{C} = \int_{C} {}^{l}\mathbf{T}_{g}^{T} \cdot \mathbf{K}^{-1} \cdot {}^{l}\mathbf{T}_{g} \cdot ds \tag{3.11}$$

The matrix $^{g}\mathbf{C}$ is the compliance matrix for a general cantilever curved beam loaded at the free end and represents the relationship between the applied loads at the beam free end and the corresponding deformations. Applying this method for a general cantilever curved beam (Fig. 3.3) with constant cross section, matrix $^{g}\mathbf{C}$ can be computed as the following:

$$^{g}\mathbf{C} = \begin{bmatrix} C_{x,f_x} & C_{x,f_y} & 0 & 0 & 0 & C_{x,m_z} \\ C_{y,f_x} & C_{y,f_y} & 0 & 0 & 0 & C_{y,m_z} \\ 0 & 0 & C_{z,f_z} & C_{z,m_x} & C_{z,m_y} & 0 \\ 0 & 0 & C_{\theta_x,f_z} & C_{\theta_x,m_x} & C_{\theta_x,m_y} & 0 \\ 0 & 0 & C_{\theta_y,f_z} & C_{\theta_y,m_x} & C_{\theta_y,m_y} & 0 \\ C_{\theta_z,f_x} & C_{\theta_z,f_y} & 0 & 0 & 0 & C_{\theta_z,m_z} \end{bmatrix} \tag{3.12}$$

The analytical expression of the matrix entries are reported in Table 3.1.

Table 3.1: Compliance factors for the cantilever curved beam loaded at the free end

$$C_{x,f_x} = -\frac{R\left(-AR^2(3\theta+\sin(\theta)(\cos(\theta)-4))-I_n\left(EA^2Gb_m(\theta-\sin(\theta)\cos(\theta))+\theta+\sin(\theta)\cos(\theta)\right)\right)}{2EAI_n}$$

$$C_{x,f_y} = C_{y,f_x} = \frac{R\left((\cos(\theta)-1)\left(-AR^2(\cos(\theta)-1)+I_n(\cos(\theta)+1)\left(EA^2Gb_m-1\right)\right)\right)}{2EAI_n}$$

$$C_{x,m_z} = C_{\theta_z,f_x} = \frac{R^2(\sin(\theta)-\theta)}{EI_n}$$

$$C_{y,f_y} = \frac{R\left(EA^2GI_nb_m(\theta+\sin(\theta)\cos(\theta))+\left(AR^2+I_n\right)(\theta-\sin(\theta)\cos(\theta))\right)}{2EAI_n}$$

$$C_{y,m_z} = C_{\theta_z,f_z} = -\frac{R^2(\cos(\theta)-1)}{EI_n}$$

$$C_{z,f_z} = \frac{R\left(GJR^2(\theta-\sin(\theta)\cos(\theta))+\frac{1}{2}EI_m\left(4AG^2\theta Jb_n+R^2(6\theta-8\sin(\theta)+\sin(2\theta))\right)\right)}{2EGJI_m}$$

$$C_{z,m_x} = C_{\theta_x,f_z} = \frac{R^2(GJ(\theta-\sin(\theta)\cos(\theta))+EI_m(\theta+\sin(\theta)(\cos(\theta)-2)))}{2EGJI_m}$$

$$C_{z,m_y} = C_{\theta_y,f_z} = -\frac{R^2\left(-GJ\cos^2(\theta)+GJ+4EI_m\sin^4\left(\frac{\theta}{2}\right)\right)}{2EGJI_m}$$

$$C_{\theta_x,m_x} = \frac{R(GJ(\theta-\sin(\theta)\cos(\theta))+EI_m(\theta+\sin(\theta)\cos(\theta)))}{2EGJI_m}$$

$$C_{\theta_x,m_y} = C_{\theta_y,m_x} = \frac{\sin^2(\theta)R(-GJ+EI_m)}{2EGJI_m}$$

$$C_{\theta_y,m_y} = -\frac{R(-GJ(\theta+\sin(\theta)\cos(\theta))+EI_m(\sin(\theta)\cos(\theta)-\theta))}{2EGJI_m}$$

$$C_{\theta_z,m_z} = \frac{\theta R}{EI_n}$$

3.3 Evaluating the Spatial Compliance of Circularly Curved-Beam Flexures

The proposed method is applied to a CCBF with radius R and angle θ with its center located at O_0 (Fig. 3.4), in order to estimate its compliant behavior under a generalized loading condition.
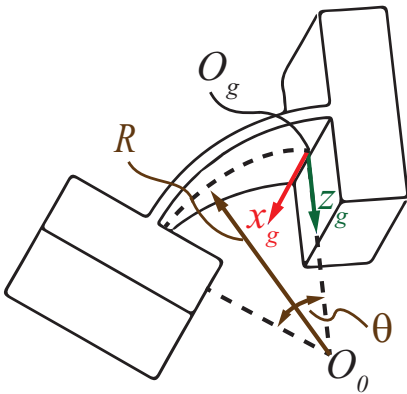
Figure 3.4: Geometric parameters of the CCBF
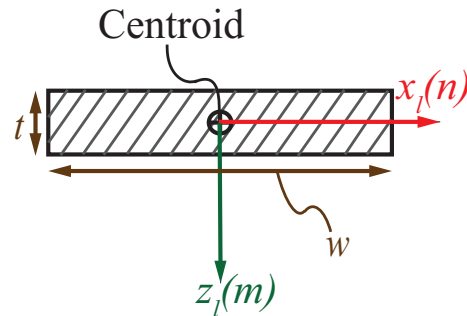
Figure 3.5: Cross section properties of the CCBF

The cross section properties of the flexure is depicted in Fig. 3.5. The CCBF compliance matrix is derived in its analytical form:

$$
{}^g\mathbf{C} = \begin{bmatrix}
C_{x,f_x} & 0 & 0 & 0 & C_{x,m_y} & C_{x,m_z} \\
0 & C_{y,f_y} & C_{y,f_z} & C_{y,m_x} & 0 & 0 \\
0 & C_{z,f_y} & C_{z,f_z} & C_{z,m_x} & 0 & 0 \\
0 & C_{\theta_x,f_y} & C_{\theta_x,f_z} & C_{\theta_x,m_x} & 0 & 0 \\
C_{\theta_y,f_x} & 0 & 0 & 0 & C_{\theta_y,m_y} & C_{\theta_y,m_z} \\
C_{\theta_z,f_x} & 0 & 0 & 0 & C_{\theta_z,m_y} & C_{\theta_z,m_z}
\end{bmatrix}
\tag{3.13}
$$

The analytical expression of the matrix entries are reported in Table 3.2. Shear induced deformations are neglected, due to the slender structure of the flexure. It can be noticed that each compliance factor is written in terms of the cross section area, principal and polar moments of inertia (namely A, I_m, I_n, and J). For a rectangular cross section, this terms can be assessed as follows:

$$
A = wt, \quad I_m = \frac{1}{12} tw^3, \quad I_n = \frac{1}{12} wt^3, \quad J = I_m + I_n = \frac{1}{12} wt \left(t^2 + w^2\right)
\tag{3.14}
$$

Table 3.2: Compliance factors for the CCBF loaded at the free end

$C_{x,f_x} = 1/2 \dfrac{R^3\left(3EI_m\theta - 4EI_m\sin(\theta) + EI_m\cos(\theta)\sin(\theta) - GJ\cos(\theta)\sin(\theta) + GJ\theta\right)}{GJEI_m}$
$C_{y,m_x} = C_{\theta_x,f_y} = -\dfrac{R^2(-\theta + \sin(\theta))}{EI_n}$
$C_{x,m_y} = C_{\theta_y,f_x} = -1/2 \dfrac{R^2\left(-2EI_m\sin(\theta) + EI_m\cos(\theta)\sin(\theta) + EI_m\theta - GJ\cos(\theta)\sin(\theta) + GJ\theta\right)}{GJEI_m}$
$C_{z,m_x} = C_{\theta_x,f_z} = -\dfrac{R^2(-1 + \cos(\theta))}{EI_n}$
$C_{x,m_z} = C_{\theta_z,f_x} = -1/2 \dfrac{R^2\left(EI_m + GJ + EI_m(\cos(\theta))^2 - 2EI_m\cos(\theta) - (\cos(\theta))^2 GJ\right)}{GJEI_m}$
$C_{\theta_x,m_x} = \dfrac{R\theta}{EI_n}$
$C_{y,f_y} = 1/2 \dfrac{R\left(I_n\cos(\theta)\sin(\theta) + I_n\theta + 3R^2A\theta - 4R^2A\sin(\theta) + R^2A\cos(\theta)\sin(\theta)\right)}{EAI_n}$
$C_{\theta_y,m_y} = 1/2 \dfrac{R(EI_m\cos(\theta)\sin(\theta) + EI_m\theta - GJ\cos(\theta)\sin(\theta) + GJ\theta)}{GJEI_m}$
$C_{y,f_z} = C_{z,f_y} = 1/2 \dfrac{R\left(-I_n + R^2A + (\cos(\theta))^2 I_n + R^2A(\cos(\theta))^2 - 2R^2A\cos(\theta)\right)}{EAI_n}$
$C_{\theta_y,m_z} = C_{\theta_z,m_y} = 1/2 \dfrac{R(EI_m - GJ)\left(-1 + (\cos(\theta))^2\right)}{GJEI_m}$
$C_{z,f_z} = -1/2 \dfrac{R(\cos(\theta)\sin(\theta) - \theta)\left(I_n + R^2A\right)}{EAI_n}$
$C_{\theta_z,m_z} = -1/2 \dfrac{R(EI_m\cos(\theta)\sin(\theta) - EI_m\theta - GJ\cos(\theta)\sin(\theta) - GJ\theta)}{GJEI_m}$

3.4   Numerical Example and Model Validation

As a case study, the compliant behavior of the CCBF and of the SBF depicted in Fig. 3.1 and Fig. 3.2 are numerically evaluated. As for the CCBF, the following geometric parameters are considered, namely $R = 30mm, t = 1.2mm, w = 6mm$ and $\theta = \pi/4$. The flexure hinge connects two rigid links located at a distance $l = 2R\sin(\theta/2)$ and is made of Acrylic Plastic with Young's modulus $E = 3000Mpa$, Poisson's ratio $v = 0.33$, shear modulus $G = 1130Mpa$. The principal hinge compliance [27] for the considered application is $C_{\theta_x,m_x} = 12R\theta/Ewt^3 = 9rad/Nm$. The method described in previous section is used for computing the overall CCBF compliance matrix, whereas FEA is performed in order to validate the theoretical model. Fig. 3.6 depicts, as an example, the CCBF undeformed and deformed shapes when subject to a flexural moment applied on the hinge free end.

Similar FEA simulations are carried out by individually loading the CCBF at the free end for each component of the load **P** (that is individual forces and moments are applied) and obtaining the corresponding deformations (displacements and rotations). The ratio between each load and deformation component simply represents the compliance factors along different axes. The overall numerical results are shown in Table 3.3, which also depicts the percentage error between analytical and FEA methods. A maximum percentage error of less than 3% confirms the validity of the proposed modeling technique.

The same procedure is then applied to compute the SBF compliance matrix whose analytical solution is known from the literature [18]. As said, the SBF is designed so as to connect the same rigid links of the previous example and to provide the same principal compliance as the CCBF previously modeled. Henceforth, the SBF length is $l = 2R\sin(\theta/2)$, the SBF principal compli-
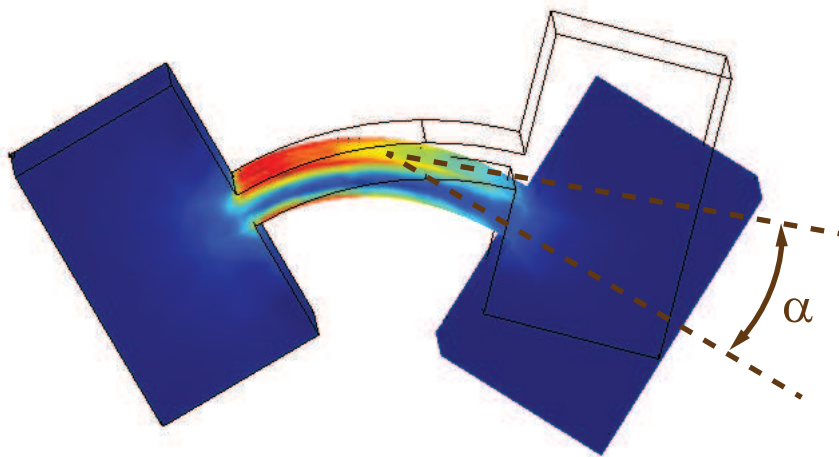
Figure 3.6: FEA of the CCBF

Table 3.3: Compliance factors for the CCBF and comparison between analytical and FEA results

Compliance factors	C_{x,f_x}	$C_{x,m_y} = C_{\theta_y,f_x}$	$C_{x,m_z} = C_{\theta_z,f_x}$	C_{y,f_y}	$C_{y,f_z} = C_{z,f_y}$	C_{θ_x,m_x}
Analytic	8.001e-5	3.016e-4	-5e-3	1.466e-4	4.483e-4	9.0903
FEA	7.746e-5	3.015e-4	-4.99e-3	1.457e-4	4.457e-4	9.0897
Percentage error	3.3	4.7e-2	6e-2	5.9e-1	5.8e-1	4.9e-4
Compliance factors	C_{z,f_z}	$C_{z,m_x} = C_{\theta_x,f_z}$	$C_{y,m_x} = C_{\theta_x,f_y}$	C_{θ_y,m_y}	$C_{\theta_y,m_z} = C_{\theta_z,m_y}$	C_{θ_z,m_z}
Analytic	1.5e-3	1.017e-1	2.72e-2	8.256e-1	-1.797e-1	4.662e-1
FEA	1.486e-3	1.017e-1	2.72e-2	8.271e-1	-1.803e-1	4.664e-1
Percentage error	3.4e-1	0	0	1.8e-1	3.2e-1	4.5e-2

ance is $\overline{C}_{\theta_x,m_x} = 12l/Ew\bar{t}^3 = 9\,rad/Nm$, whereas the SBF thickness, $\bar{t}$, is chosen accordingly as $\bar{t} = t\left(2\sin(\theta/2)/\theta\right)^{1/3}$.

The numerical values of the compliance matrix entries are depicted in Fig. 3.7 and Fig. 3.8 respectively. Similarly to [27], this 3D bar graph representation allows a qualitative comparison of the hinge behavior in terms of selective compliance. It can be noticed that, in this particular case, the two solutions behave similarly. However, CCBF outperforms SBF in terms of maximum achievable principal rotation. The maximum principal rotation before failure is limited by the employed material yield strength S_y. Concerning CCBF, the maximum principal rotation is given by [18]:

$$\alpha_{CCBF} = max(\alpha_1, \alpha_2) \tag{3.15}$$

where:

$$\alpha_1 = \frac{6R(t+R)S_y\theta\left(-2t + (t+2R)\mathrm{Log}\left[\frac{t+R}{R}\right]\right)}{t^2 E\left(-t + (t+R)\mathrm{Log}\left[\frac{t+R}{R}\right]\right)} \tag{3.16}$$

$$\alpha_2 = 6E^{-1}RS_y\theta\left(\frac{t+2R}{t^2} + \frac{1}{-t + R\mathrm{Log}\left[\frac{t+R}{R}\right]}\right) \tag{3.17}$$

Note that the switching condition of Eq. 3.15 is due to the fact that, depending on the hinge dimensions, the highest stress may occur at either inner or outer surface.

Concerning SBF, the maximum principal rotation is given by:

$$\alpha_{SBF} = 2\frac{t}{l}\frac{S_y}{E} \tag{3.18}$$

A comparison in terms of maximum achievable rotation can be made by computing $\alpha_{CCBF}/\alpha_{SBF}$. In particular, Fig. 3.9 depicts the comparison of the maximum achievable rotation as a function of the CCBF radius, $R \in [20-40]mm$, and thickness, $t \in [0.5-3]mm$ (for $\theta = \frac{1}{4}\pi$). Note that the value of $\alpha_{CCBF}/\alpha_{SBF}$ does not depend on the hinge width, w. The comparison clearly shows that CCBF must be preferred in terms of principal rotation capabilities as long as $\alpha_{CCBF}/\alpha_{SBF} > 1$.
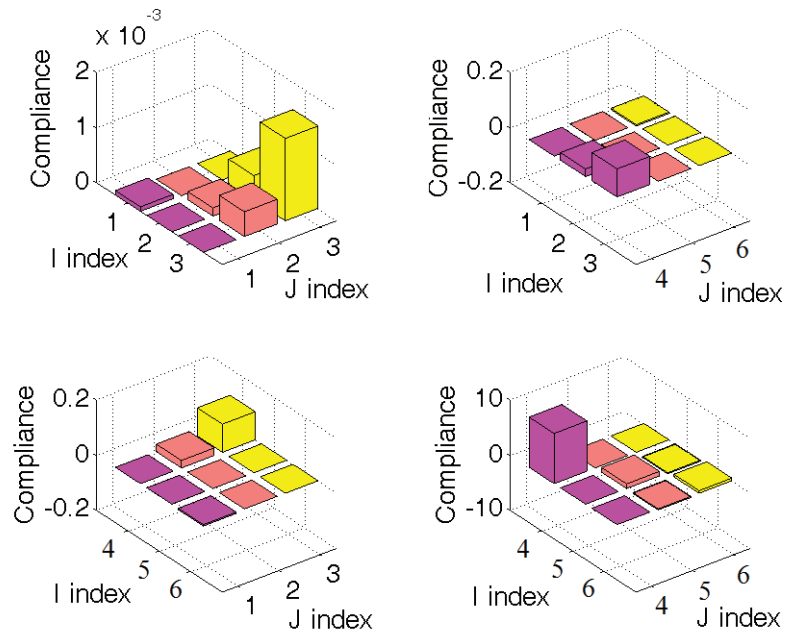
Figure 3.7: 3D bar representation for the compliance matrix of the CCBF
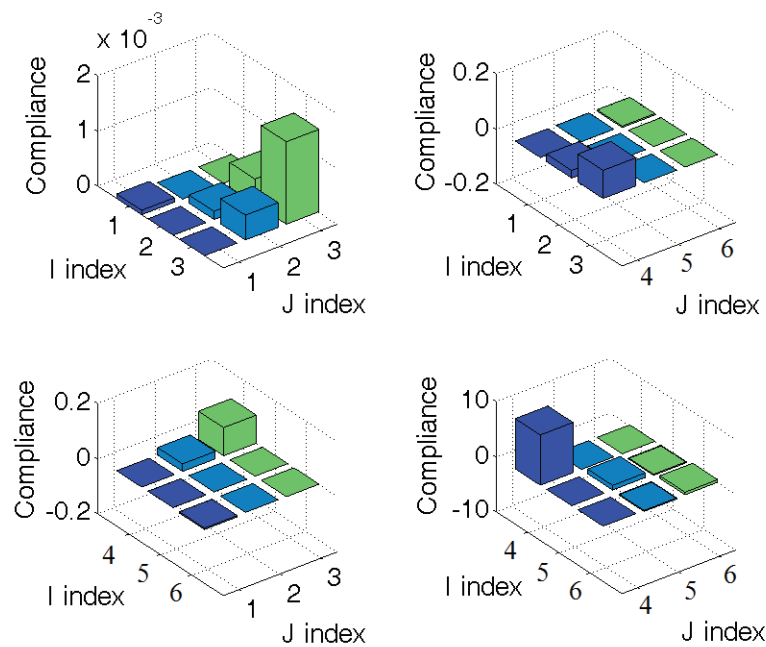
Figure 3.8: 3D bar representation for the compliance matrix of the SBF
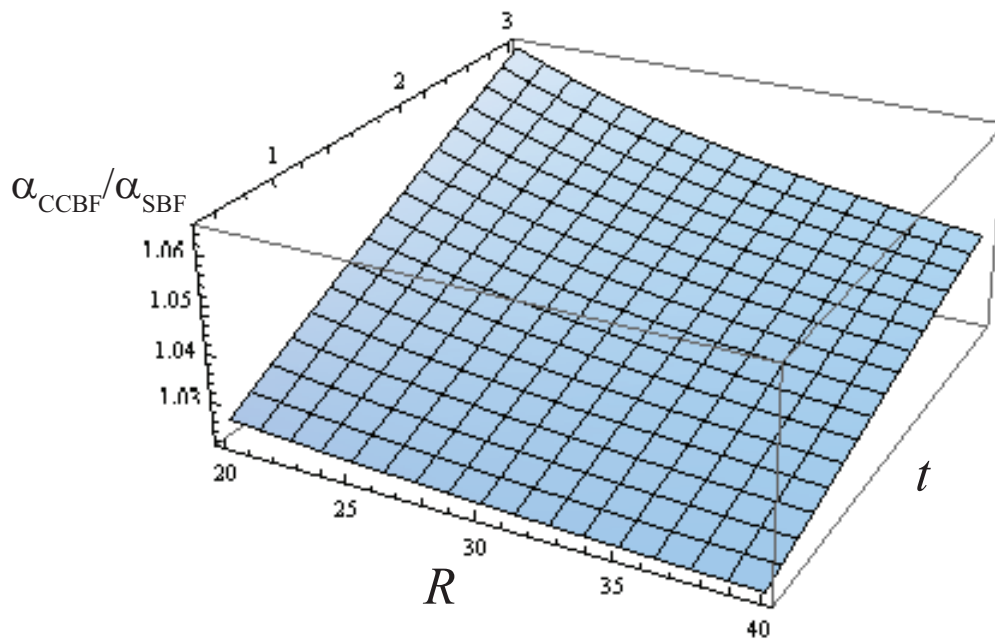
Figure 3.9: Comparison of the maximum achievable rotation, $\alpha_{CCBF}/\alpha_{SBF}$, as a function of the CCBF radius, R, and thickness, t.

Chapter 4

Design and Characterization of Spherical Flexure Hinges for Spatial Compliant Mechanisms

In this chapter, the closed-form compliance equations for spherical flexures are derived. Each element of the spatial compliance matrix is analytically computed as a function of both hinge dimensions and employed material. The theoretical model is then validated by relating analytical data with the results obtained through finite element analysis. Finally, for a generic loading condition, spherical flexures are compared to circularly curved-beam flexures in terms of secondary compliance factors and maximum stress.

4.1 Introduction

Most of the aforementioned flexures discussed in previous chapters have been specifically applied and conceived for prevalent planar motions only. Despite the practical relevance, investigations on flexure hinges particularly designed for spatial motions are instead quite limited. For instance, Lobontiu et al. [32, 33] investigated the two- and three-axis flexure hinges. The former consists of two collocated notches that are cut perpendicular to each other; the latter consists of an axial-symmetric notch. In both cases, the resulting hinge features a small cross-sectional area and is prone to unintentional rotations or buckling even when loaded with small forces. Jagirdar [34] used PRBM to study the kinematics and elasticity of curved beams. Li and Chen [35] employed two CCBFs with rectangular cross-section to devise a spherical Young parallel mechanism using

PRBM. Considering the fact that a flexure hinge should be compliant about its principle compliant axis (axes) and as stiff as possible in other directions, this characteristic can be achieved for spherical motions, by using CCBFs that are compliant along their curve with respect to the axes intersecting in the center of the sphere.

In this chapter, Spherical Flexures (SFs) have been specifically designed and evaluated for prevalent spherical motions in spherical compliant mechanisms and are compared in terms of parasitic motions and maximum stress to CCBFs with rectangular cross section that feature equivalent compliant behavior with respect to moment-induced rotations.

The relevant contribution of this chapter will be published in [36].

4.2   Closed-Form Compliance Equations for Spherical Flexure Hinges

A SF features an arc of a circle as centroidal axis and an annulus sector as cross-section. Circle and annulus have a common center coinciding to that of the desired spherical motion. The axis of the smaller SF central moment of inertia points towards the desired center of spherical motion. With reference to Fig. 4.1, let us consider a SF with subtended centroidal radius R and angle θ with the center located at O_0. The flexure is loaded at its free end denoted by a global frame with corresponding axes x_g, y_g, z_g and origin point O_g centered at hinge cross section centroid. Following the general approach described in Section 3.2, the compliance matrix for the SF, can be
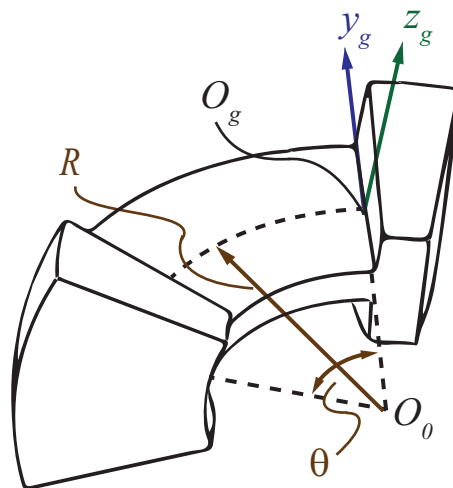
Figure 4.1: Geometric parameters of the SF

obtained as follows:

$$
{}^g\mathbf{C} = \begin{bmatrix}
C_{x,f_x} & C_{x,f_y} & 0 & 0 & 0 & C_{x,m_z} \\
C_{y,f_x} & C_{y,f_y} & 0 & 0 & 0 & C_{y,m_z} \\
0 & 0 & C_{z,f_z} & C_{z,m_x} & C_{z,m_y} & 0 \\
0 & 0 & C_{\theta_x,f_z} & C_{\theta_x,m_x} & C_{\theta_x,m_y} & 0 \\
0 & 0 & C_{\theta_y,f_z} & C_{\theta_y,m_x} & C_{\theta_y,m_y} & 0 \\
C_{\theta_z,f_x} & C_{\theta_z,f_y} & 0 & 0 & 0 & C_{\theta_z,m_z}
\end{bmatrix}
\tag{4.1}
$$

Neglecting shear deformations, being a slender beam, the compliance factors for the matrix ${}^g\mathbf{C}$ is reported in Table 4.1. Each compliance factor is written in terms of the cross section area, area and polar moments of inertia (namely A, I_m, I_n, and J). In particular, these properties are derived as a function of the SF geometric parameters in the following section.

4.3 Defining Cross Section Properties for the Spherical Flexure

In particular, the SF cross section is an annular sector (Fig. 4.2), that can be considered as the common section of two concentric circular sectors with different radius. Let us consider r_i and r_o as the radius of the inner and the outer circular sectors respectively. Assuming β as the subtended

Table 4.1: Compliance factors for the SF loaded at the free end

$C_{x,f_x} = \dfrac{R\left(A\cos(\theta)\sin(\theta)R^2 - 4A\sin(\theta)R^2 + 3AR^2\theta + \cos(\theta)\sin(\theta)I_n + I_n\theta\right)}{2EAI_n}$
$C_{x,f_y} = C_{y,f_x} = -\dfrac{R\left(A(\cos(\theta))^2 R^2 - 2R^2 A\cos(\theta) + R^2 A + (\cos(\theta))^2 I_n - I_n\right)}{2EAI_n}$
$C_{x,m_z} = C_{\theta_z,f_x} = \dfrac{R^2(\sin(\theta) - \theta)}{EI_n}$
$C_{y,f_y} = -\dfrac{R(\cos(\theta)\sin(\theta) - \theta)\left(R^2 A + I_n\right)}{2EAI_n}$
$C_{y,m_z} = C_{\theta_z,f_y} = -\dfrac{R^2(\cos(\theta) - 1)}{EI_n}$
$C_{z,f_z} = \dfrac{R^3(EI_m\cos(\theta)\sin(\theta) - GJ\cos(\theta)\sin(\theta) - 4EI_m\sin(\theta) + 3EI_m\theta + GJ\theta)}{2GJEI_m}$
$C_{z,m_x} = C_{\theta_x,f_z} = \dfrac{R^2(EI_m\cos(\theta)\sin(\theta) - GJ\cos(\theta)\sin(\theta) - 2EI_m\sin(\theta) + EI_m\theta + GJ\theta)}{2GJEI_m}$
$C_{z,m_y} = C_{\theta_y,f_z} = -\dfrac{R^2\left(EI_m(\cos(\theta))^2 - GJ(\cos(\theta))^2 - 2EI_m\cos(\theta) + EI_m + GJ\right)}{2GJEI_m}$
$C_{\theta_x,m_x} = \dfrac{R(EI_m\cos(\theta)\sin(\theta) - GJ\cos(\theta)\sin(\theta) + EI_m\theta + GJ\theta)}{2GJEI_m}$
$C_{\theta_x,m_y} = C_{\theta_y,m_x} = \dfrac{R(EI_m - GJ)(\sin(\theta))^2}{2GJEI_m}$
$C_{\theta_y,m_y} = -\dfrac{R(EI_m\cos(\theta)\sin(\theta) - GJ\cos(\theta)\sin(\theta) - EI_m\theta - GJ\theta)}{2GJEI_m}$
$C_{\theta_z,m_z} = \dfrac{R\theta}{EI_n}$
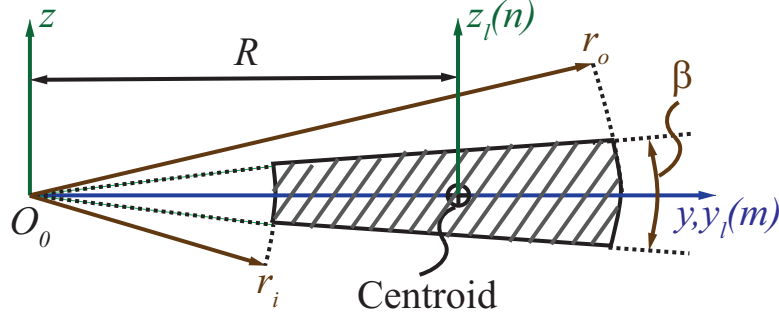
Figure 4.2: Cross section properties of the SF

angle of the annular sector, the cross section area can be obtained by using definite integration over the annular sector as follows:

$$A = \int\limits_{-\beta/2}^{\beta/2} \int\limits_{r_i}^{r_o} r\,dr\,d\beta = \frac{r_o^2 \beta}{2} - \frac{r_i^2 \beta}{2} = \frac{(r_o^2 - r_i^2)\beta}{2} \tag{4.2}$$

In order to derive area and polar moments of inertia with respect to the centroidal axis, we need to locate the centroid of the annular cross section. Using the definition for the first moment of area, one can obtain:

$$S_y = A\bar{z} = \int_A z\,dA = \int\limits_{-\beta/2}^{\beta/2} \int\limits_{r_i}^{r_o} (r\sin\beta)r\,dr\,d\beta = 0 \Rightarrow \bar{z} = S_y/A = 0 \tag{4.3}$$

$$S_z = A\bar{y} = \int_A y\,dA = \int\limits_{-\beta/2}^{\beta/2} \int\limits_{r_i}^{r_o} (r\cos\beta)r\,dr\,d\beta = \frac{2}{3}(r_o^3 - r_i^3)\sin\beta/2$$

$$\Rightarrow \bar{y} = S_z/A = \frac{4}{3}\frac{(r_o^3 - r_i^3)\sin\beta/2}{(r_o^2 - r_i^2)\beta} = R \tag{4.4}$$

where S_y and S_z are the first moments of area about y and z axes. The area moments of inertia with respect to y and z axes, can then be written as:

$$I_y = \int_A z^2\,dA = \int\limits_{-\beta/2}^{\beta/2} \int\limits_{r_i}^{r_o} (r\sin\beta)^2 r\,dr\,d\beta = \frac{1}{8}(r_o^4 - r_i^4)(\beta - \sin\beta) \tag{4.5}$$

$$I_z = \int_A y^2 \, dA = \int_{-\beta/2}^{\beta/2} \int_{r_i}^{r_o} (r\cos\beta)^2 r \, dr \, d\beta = \frac{1}{8}(r_o^4 - r_i^4)(\beta + \sin\beta) \tag{4.6}$$

By applying parallel axis theorem [37], one can find the area and polar moments of inertia with respect to the centroidal axis, transfering them from y and z to y_l and z_l axes:

$$I_m = I_y = \frac{1}{8}(r_o^4 - r_i^4)(\beta - \sin\beta) \tag{4.7}$$

$$I_n = I_z - AR^2 = \frac{1}{8}(r_o^4 - r_i^4)(\beta + \sin\beta) - \frac{8}{9}\frac{(r_o^3 - r_i^3)^2 \sin^2(\beta/2)}{(r_o^2 - r_i^2)\beta} \tag{4.8}$$

$$J = I_m + I_n = \frac{1}{4}(r_o^4 - r_i^4)\beta - \frac{8}{9}\frac{(r_o^3 - r_i^3)^2 \sin^2(\beta/2)}{(r_o^2 - r_i^2)\beta} \tag{4.9}$$

Replacing Eqs. 4.2, 4.7, 4.8 and 4.9 in Table 4.1, the compliance matrix for the SF will be determined as a function of the hinge geometric parameters and the applied material.

4.4 Stress Considerations

Stress distribution over different cross sections of a flexure hinge is the result of normal stresses that are produced through bending and tension/compression, and tangential stresses that are produced through torsion [22]. Considering the von Mises criterion for plane stress condition, the maximum stress occurs at any cross section of the flexure hinge, can be expressed as:

$$\sigma_{max} = \sqrt{(\sigma^2 + 3\tau^2)_{max}} \tag{4.10}$$

Curved beam theories i.e. Winkler-Bach formula should have been considered to evaluate stress distribution of curved flexuers [38]. However, we are generally interested in knowing the maximum stress in the flexure. In order to fulfill this goal, we use stress concentration factors that were proposed by Wilson and Quereau [39] conducting a numerous strings of experiments on curved beams with various cross sections to simplify the procedure of determining stress in this type of flexural members.

Let us consider the SF depicted in Fig. 4.1 loaded with a generic load ${}^g\mathbf{w} = [f_x\, f_y\, f_z\, m_x\, m_y\, m_z]^T$ at its free end. Maximum stress terms across an arbitrary cross section of the flexure can be written as:

$$\sigma_{max} = \max\left(\frac{km_n y_l}{I_n} + \frac{km_m z_l}{I_m} + \frac{kf_l}{A}\right) \tag{4.11}$$

$$\tau_{max} = \frac{km_l\sqrt{y_l^2 + z_l^2}}{J} \tag{4.12}$$

where:

$$f_l = f_x \cos(\theta) + f_y \sin(\theta)$$

$$m_l = -f_z R(1 - \cos(\theta)) + m_x \cos(\theta) + m_y \sin(\theta)$$

$$m_n = -f_x R(1 - \cos(\theta)) + m_z + f_y R \sin(\theta)$$

$$m_m = -f_z R(\sin(\theta) - m_x \sin(\theta) + m_y \cos(\theta)$$

y_l and z_l are the maximum longitudinal and transversal lengths measured from the cross section centroid. Considering the cross section symmetry, these lengths could encompass positive or negative quantities based on the loading profile. k is the empirical formula for stress correction factors for curved flexures and can be obtained from [39]:

$$k = 1 + 0.5 \frac{I_n}{bc^2} \left\{ \frac{1}{R - c} + \frac{1}{R} \right\} \tag{4.13}$$

where:

b = maximum breadth of section

c = distance from centroidal axis to the inner fiber

In applications that the loading is not known or fully determined but the deformation of the flexure free end is specified, the recent stress equations can be expressed in the displacement domain using the following transformation between compliance and stiffness matrices:

$$^g\mathbf{w} = {}^g\mathbf{K}.{}^g\mathbf{s}; \quad {}^g\mathbf{K} = {}^g\mathbf{C}^{-1} \tag{4.14}$$

where $^g\mathbf{s}$ is the deformation of the flexure free end in the global coordinate system.

4.5   Numerical Example and Model Validation

The SF depicted in Fig. 4.1 is considered as a case study. The geometric parameters employed in the simulation are $ro = 60mm, ri = 50mm, \theta = \pi/3$ and $\alpha = \pi/180$. The hinge is made of Acrylic Plastic with Young's modulus $E = 3000MPa$ and Poisson's ratio $v = 0.33$. The aforementioned theoretical procedure is adopted to estimate the SF compliance matrix. Results are then validated through FEA performed with the commercial software COMSOL (Fig. 4.3). Table 4.2 compares the results obtained via numerical model and FEA. The comparison shows a close agreement between the two methods.

In order to evaluate the flexure performance, we have compared the aforementioned SF with a rectangular cross section CCBF having identical centroidal axes and subtended angles. In addition, the two flexures are suitably dimensioned in order to present the same compliant behavior with respect to moment-induced rotations. The resulting CCBF width and thickness are $w = 9.98mm$ and $t = 0.963mm$. By applying the method described in Section 3.3, the CCBF compliance matrix
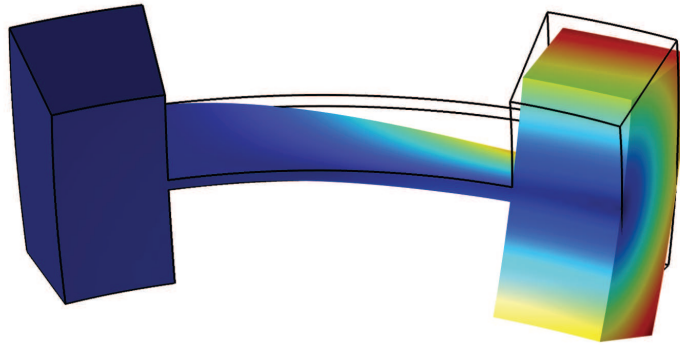
Figure 4.3: FEA of the SF

has been computed and numerical data are shown in Table 4.3. As we can see, the compliance factors become identical for the two flexures with the exception of C_{x,f_x}, C_{x,f_y} and C_{y,f_x}, which represent undesired (secondary) compliances in all those application requiring a spherical motion. Naturally, unavoidable secondary compliances should be minimized in order to decrease parasitic motions as much as possible. A quantitative comparison between SF and CCBF can then be achieved by defining two compliance ratios as follows:

$$r_{x,x} = \frac{C_{x,f_x}^{SF}}{C_{x,f_x}^{CCBF}}; \quad r_{x,y} = \frac{C_{x,f_y}^{SF}}{C_{x,f_y}^{CCBF}} = \frac{C_{y,f_x}^{SF}}{C_{y,f_x}^{CCBF}} \tag{4.15}$$

where each SF compliance factor (referred to with SF superscript) is divided by the corresponding CCBF compliance factor (referred to with CCBF superscript). In order to understand the behavior of SFs and CCBFs in terms of parasitic motions, we have assessed the influence of the geometric parameters on these two factors. This goal is achieved by evaluating the compliance ratios $r_{x,x}$

Table 4.2: Compliance factors for the SF and comparison between analytical and FEA results

Compliance factors	C_{x,f_x}	$C_{x,f_y} = C_{y,f_x}$	$C_{x,m_z} = C_{\theta_z,f_x}$	C_{y,f_y}	$C_{y,m_z} = C_{\theta_z,f_y}$	C_{z,f_z}
Analytic	4.0146e-5	-8.6900e-5	-0.0023	2.1584e-4	0.0064	0.0232
FEA	4.0149e-5	-8.6947e-5	-0.0023	2.1594e-4	0.0064	0.0232
Percentage error	7.5e-3	0.054	0	0.046	0	0
Compliance factors	C_{θ_x,m_x}	$C_{z,m_x} = C_{\theta_x,f_z}$	$C_{x,m_y} = C_{\theta_y,f_z}$	C_{θ_y,m_y}	$C_{\theta_x,m_y} = C_{\theta_y,m_x}$	C_{θ_z,m_z}
Analytic	8.0448	0.4147	-0.5158	18.4932	-9.0486	0.2413
FEA	8.0466	0.4148	-0.5159	18.4966	-9.0492	0.2413
Percentage error	0.022	0.024	0.019	0.018	6.6e-3	0

Table 4.3: Compliance factors for the similar CCBF

Compliance elements	C_{x,f_x}	$C_{x,f_y} = C_{y,f_x}$	$C_{x,m_z} = C_{\theta_z,f_x}$	C_{y,f_y}	$C_{y,m_z} = C_{\theta_z,f_y}$	C_{z,f_z}
Value	4.0144e-5	-8.6901e-5	-0.0023	2.1584e-4	0.0064	0.0232

Compliance elements	C_{θ_x,m_x}	$C_{z,m_x} = C_{\theta_x,f_z}$	$C_{x,m_y} = C_{\theta_y,f_z}$	C_{θ_y,m_y}	$C_{\theta_x,m_y} = C_{\theta_y,m_x}$	C_{θ_z,m_z}
Value	8.0448	0.4147	-0.5158	18.4932	-9.0486	0.2413

and $r_{x,y}$ for varying values of R and θ. Fig. 4.4 and Fig. 4.5 respectively represent the values $(1 - r_{x,x}) \times 100$ and $(1 - r_{x,y}) \times 100$ as function of R and θ. From these two graphs, $r_{x,y}$ is always negative whereas r_{x,f_x} is always positive, meaning that it is impossible to assess which flexure presents the best selectively compliant behavior without considering a specific loading condition. It is also worth mentioning that by increasing the length of the flexures, the ratios $r_{x,x}$ and $r_{x,y}$ are tending to 1, which imply a similar deformation behavior for relatively large length-to-thickness ratios. For what concerns the overall Von Mises stress on each flexure when loaded with a (principal) bending moment m_y on the free end, the following stress ratio has been defined:

$$r_\sigma = \frac{\sigma_{max}^{SF}}{\sigma_{max}^{CCBF}} \tag{4.16}$$

We have obtained this ratio for varying values of R and θ. In particular, the ratio r_σ assumes a constant value equaling 0.918 at varying R whereas the influence of θ is shown in Fig. 4.6. As we can see, SF outperforms CCBF, being characterized by a lower stress level for equal load (meaning that the SF outperforms CCBF in terms of maximum achievable rotation).
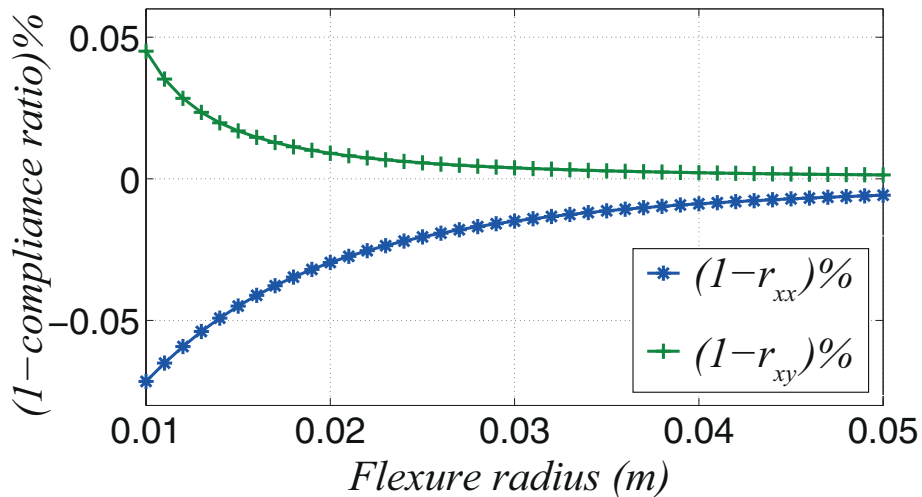
Figure 4.4: Influence of varying R on compliance ratios
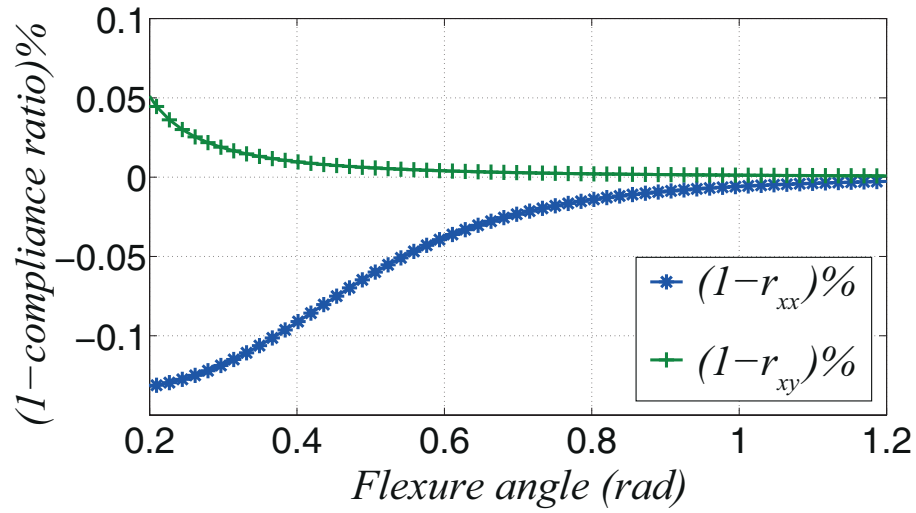
Figure 4.5: Influence of varying θ on compliance ratios
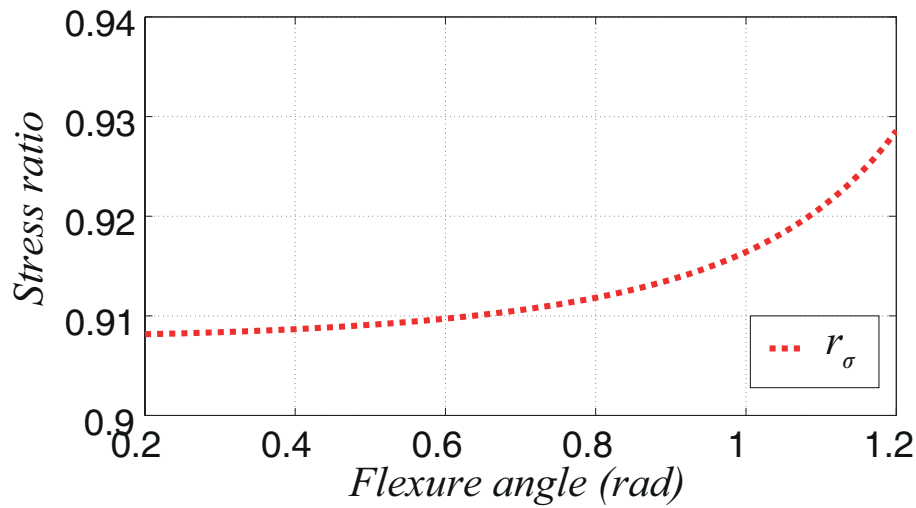
Figure 4.6: Influence of varying θ on stress ratio

Chapter 5

Compliance-Based Evaluation of a Fully Compliant Spherical Chain with Two Degrees of Freedom

This chapter introduces and investigates a fully compliant spherical chain that is obtained by the in-series connection of two identical primitive spherical flexures with coincident center of spherical motion. The compliance matrix of the proposed chain is obtained via an analytical procedure and validated via finite element analysis. Comparison with an equivalent fully compliant chain employing straight beam flexures is also provided to highlight the added benefits when using primitive spherical flexures.

5.1 Introduction

Spherical mechanisms are an important class of spatial mechanisms that find vast applications in pointing/orientation systems and mechanical transmissions [40]. These mechanisms are characterized by having all points of their links moving on concentric spherical surfaces; the center of these spheres being denoted as center of spherical motion. In its simplest form, a spherical chain features the in-series connection of two or more revolute pairs with axes intersecting in the said center of spherical motion.

Some studies have been proposed to investigate compliant mechanisms involving spatial motions as well as fully compliant spherical mechanisms.Smith [41] proposed compliant universal joints fabricated from circular leaf springs, which also provided axial translation for self-alignment ap-
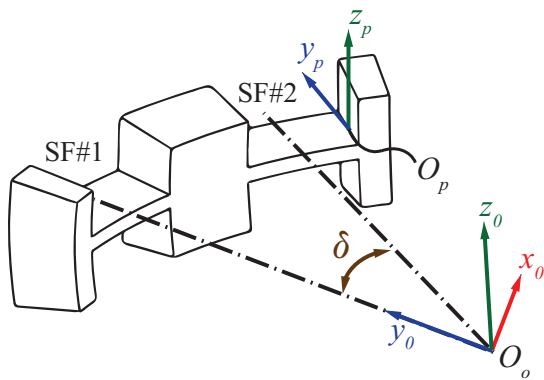
Figure 5.1: SF-based compliant chain   Figure 5.2: SBF-based compliant chain
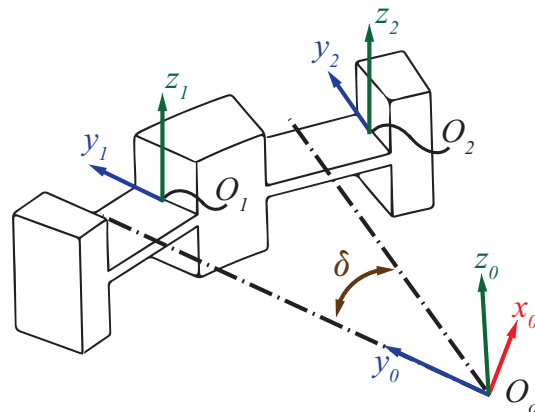
plications. However, the proposed joints are affected by significant stress concentrations that limit their ranges of motion. Moon et al. [42] developed a compliant revolute hinge based on torsion beams of cross or segmented-cross type, and employed two of them, connected in series with orthogonal axes, to conceive a fully compliant universal joint. Later on, the ensemble of two universal joints of this kind has been proposed by Machekposhti et al. [43] to obtain a compliant constant velocity Double-Hooke's universal joint. Different authors [44, 45] employed two in-series connected flexure notch hinges with orthogonal axes to conceive a fully compliant universal joint. Jacobsen et al. [46] employed three in-series connected lamina emergent torsional joints with axes intersecting in a single point to make spherical chains with three degrees of freedom (for compliant joints or mechanisms, the number of degrees of freedom is intended as the number of independent prevalent directions of motion). These spherical chains were then used to build a 3-RRR spherical parallel mechanism (R being a revelote joint). Callegari et al. [47] addressed the analysis and design of a 3-CRU spherical parallel mechanism with flexure hinges (C and U being cylindrical and universal joints respectively).

All the aforementioned studies are based on the use and proper combination of primitive flexures that are specifically conceived for prevalent planar motions only. In previous chapter, the dedicated studies to design of flexure hinges for spatial applications were addressed and SFs were specifically designed and evaluated for prevalent spherical motions in spherical compliant mechanisms. In this chapter, a fully compliant spherical chain that is made by the in-series connection of two identical primitive SFs with coinciding centers of spherical motion (Fig. 5.1). In particular, the stiffness analysis of the proposed fully compliant spherical chain is addressed. Simulation results are compared to those of a similar chain (Fig. 5.2) employing SBFs. Overall, the stiffness analysis highlights that the use of two primitive SFs makes it possible to conceive fully compliant spherical chains with two independent prevalent directions of rotation and with reduced parasitic translational motions. The relevant contribution of this chapter is submitted to [48].

5.2 Closed-Form Compliance Equations for a Serial 2-SF Spherical Chain

Concerning the frame dependency, as explained in [17], compliance matrices at different reference frames (e.g. from the frame S_p to a generic frame S_0 (Fig. 5.1)) can be related resorting to the 6*x*6 *adjoint matix* $^p\mathbf{T}_0$:

$$^p\mathbf{T}_0 = \left[\begin{array}{c:c} {}^p\mathbf{R}_0 & \mathbf{0} \\ \hdashline {}^p\widetilde{\mathbf{r}}_0 \cdot {}^p\mathbf{R}_0 & {}^p\mathbf{R}_0 \end{array} \right] = \left[\begin{array}{c:c} {}^0\mathbf{R}_p^T & \mathbf{0} \\ \hdashline \left({}^0\widetilde{\mathbf{r}}_p \cdot {}^0\mathbf{R}_p\right)^T & {}^0\mathbf{R}_p^T \end{array} \right] \tag{5.1}$$

where $^p\mathbf{R}_0$ denotes the rotation matrix of frame S_0 with respect to frame S_p (i.e. the columns of $^p\mathbf{R}_0$ are the unit vectors of frame S_0 expressed in the coordinate frame S_p), and $^0\widetilde{\mathbf{r}}_p$ denotes the skew symmetric matrix of the position vector $^p\mathbf{r}_0$, which locates the origin of frame S_0 with respect to frame S_p.

Specifically, once the compliance matrix $^p\mathbf{C}$ at frame S_p is known, the compliance matrix related to the frame S_0 can be simply calculated as:

$$^0\mathbf{C} = {}^0\mathbf{T}_p^{-T} \cdot {}^p\mathbf{C} \cdot {}^0\mathbf{T}_p^{-1} = {}^p\mathbf{T}_0^T \cdot {}^p\mathbf{C} \cdot {}^p\mathbf{T}_0 \tag{5.2}$$

where T denotes the transpose of a matrix. As reported in [49], the 6*x*6 *adjoint matrix* is also useful for characterizing a collection of n in-series connected compliant flexures. In this case, the overall system compliance can be simply obtained by summing up the compliance matrices of each flexure, once all matrices are related to a common reference frame S_0. Therefore, resorting to Eq. 5.2, the following relation holds:

$$^0\mathbf{C} = \sum_g^n {}^0\mathbf{T}_g^{-T} \cdot {}^g\mathbf{C} \cdot {}^0\mathbf{T}_g^{-1} = \sum_g^n {}^g\mathbf{T}_0^T \cdot {}^g\mathbf{C} \cdot {}^g\mathbf{T}_0 \tag{5.3}$$

In the following, the procedure is outlined for the fully compliant spherical chain depicted in Fig. 5.1. The chain is composed by the in-series connection of two SFs (hereafter referred to as SF#1 and SF#2) that are both identical to the SF represented in Chapter 4 (Fig. 4.1) with centroidal axes lying on the same circumference. The compliance matrix of each SF can then be recalled from Section 4.2. Let us denote $^1\mathbf{C}$ and $^2\mathbf{C}$ as the compliance matrix of each SF as referred to the hinge free end. The center of the spherical motion (i.e. point O_0 in Fig. 5.1) is then taken as the origin of S_0, the frame axes being oriented such that y_0 axis passes through the centroid of the SF#1 mid cross section, whereas z_0 axis is orthogonal to the symmetry plane containing the centroidal axes (similar to z axis in Fig. 4.2).

As a further step, the adjoint matrices $^1\mathbf{T}_0$ and $^2\mathbf{T}_0$, respectively relating $^1\mathbf{C}$ and $^2\mathbf{C}$ to S_0, should be computed. Recalling Eq. 5.1, the rotation matrices, $^1\mathbf{R}_0$ and $^2\mathbf{R}_0$, and the translation vectors, $^1\mathbf{r}_0$ and $^2\mathbf{r}_0$, composing $^1\mathbf{T}_0$ and $^2\mathbf{T}_0$ are defined as follows:

$$^1\mathbf{R}_0 = \begin{bmatrix} \cos(\theta/2) & -\sin(\theta/2) & 0 \\ \sin(\theta/2) & \cos(\theta/2) & 0 \\ 0 & 0 & 1 \end{bmatrix} \tag{5.4}$$

Table 5.1: Compliance elements of the mechanism

$C_{x,f_x} = -\dfrac{R\left(-2\left(AR^2+I_n\right)\left(\cos^2(\delta)\sin(\theta)+\theta\right)\right)}{2EAI_n}$	$C_{x,f_y} = C_{y,f_x} = -\dfrac{R\left(\sin(2\delta)\sin(\theta)\left(AR^2+I_n\right)\right)}{2EAI_n}$
$C_{y,f_y} = \dfrac{R\left(2\left(AR^2+I_n\right)\left(\theta-\cos^2(\delta)\sin(\theta)\right)\right)}{2EAI_n}$	$C_{x,m_z} = C_{\theta_z,f_x} = -\dfrac{R^2\left(-4\cos^2\left(\frac{\delta}{2}\right)\sin\left(\frac{\theta}{2}\right)\right)}{EI_n}$
$C_{y,m_z} = C_{\theta_z,f_z} = -\dfrac{R^2\left(2\sin(\delta)\sin\left(\frac{\theta}{2}\right)\right)}{EI_n}$	$C_{z,m_x} = C_{\theta_x,f_z} = \dfrac{R^2\left(-4\cos^2\left(\frac{\delta}{2}\right)\sin\left(\frac{\theta}{2}\right)\right)}{GJ}$
$C_{\theta_x,m_x} = -\dfrac{R\left(-2GJ\left(\theta-\cos^2(\delta)\sin(\theta)\right)-2EI_m\left(\cos^2(\delta)\sin(\theta)+\theta\right)\right)}{2EGJI_m}$	$C_{z,f_z} = 2\dfrac{R^3\theta}{GJ}$
$C_{\theta_x,m_y} = C_{\theta_y,m_x} = R\sin(\delta)\cos(\delta)\sin(\theta)\left(\frac{1}{EI_m}-\frac{1}{GJ}\right)$	$C_{z,m_y} = C_{\theta_y,f_z} = \dfrac{R^2\left(2\sin(\delta)\sin\left(\frac{\theta}{2}\right)\right)}{GJ}$
$C_{\theta_y,m_y} = \dfrac{R\left(2GJ\left(\cos^2(\delta)\sin(\theta)+\theta\right)+2EI_m\left(\theta-\cos^2(\delta)\sin(\theta)\right)\right)}{2EGJI_m}$	$C_{\theta_z,m_z} = 2\dfrac{R\theta}{EI_n}$

$$
{}^{2}\mathbf{R}_0 = \begin{bmatrix} \cos(\theta/2+\delta) & -\sin(\theta/2+\delta) & 0 \\ \sin(\theta/2+\delta) & \cos(\theta/2+\delta) & 0 \\ 0 & 0 & 1 \end{bmatrix}
\tag{5.5}
$$

$$
{}^{1}\mathbf{r}_0 = {}^{2}\mathbf{r}_0 = \begin{bmatrix} 0, & -R, & 0 \end{bmatrix}^T
\tag{5.6}
$$

where R and θ represent the radius and subtended angle of SF#1 and SF#2 centroidal axes, whereas δ is the angle between the y_0 axis and an axis connecting point O_0 and the centroid of the SF#2 mid cross section. The overall chain compliance matrix can then be computed resorting to Eq. 5.3, where $n = 2$. In particular, the matrix ${}^{0}\mathbf{C}$ can be expressed as follows:

$$
{}^{0}\mathbf{C} = \begin{bmatrix}
C_{x,f_x} & C_{x,f_y} & 0 & 0 & 0 & C_{x,m_z} \\
C_{y,f_x} & C_{y,f_y} & 0 & 0 & 0 & C_{y,m_z} \\
0 & 0 & C_{z,f_z} & C_{z,m_x} & C_{z,m_y} & 0 \\
0 & 0 & C_{\theta_x,f_z} & C_{\theta_x,m_x} & C_{\theta_x,m_y} & 0 \\
0 & 0 & C_{\theta_y,f_z} & C_{\theta_y,m_x} & C_{\theta_y,m_y} & 0 \\
C_{\theta_z,f_x} & C_{\theta_z,f_y} & 0 & 0 & 0 & C_{\theta_z,m_z}
\end{bmatrix}
\tag{5.7}
$$

Matrix ${}^{0}\mathbf{C}$ relates the wrench ${}^{0}\mathbf{w}$ acting on S_0 to the corresponding generalized displacement ${}^{0}\mathbf{s}$, (namely ${}^{0}\mathbf{s} = {}^{0}\mathbf{C} \cdot {}^{0}\mathbf{w}$). The analytical expression of the matrix entries are reported in Table 5.1 as a function of the geometric parameters and the employed material. The cross section properties (A, I_m, I_n, and J) can be recalled from Section 4.3 as a function of the hinge geometric parameters.

5.3   Numerical Example and Model Validation

A fully-compliant spherical chain featuring two identical in-series SFs is considered as a case study. The SF geometric parameters and the material employed for the simulations are identical to
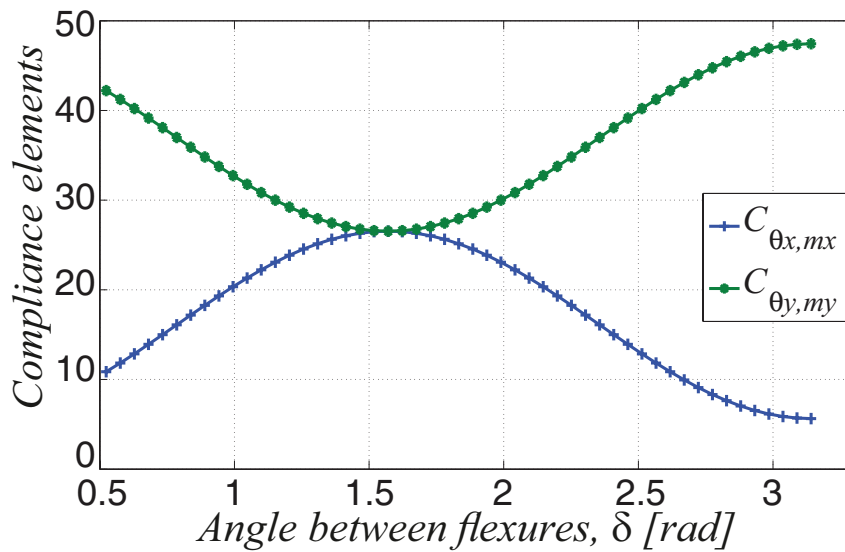
Figure 5.3: Influence of varying δ on principal compliances

the corresponding data used in Section 4.5. For a generic angle δ, the aforementioned theoretical procedure is adopted to estimate the overall compliance matrix. The dependency of the principal compliance elements, C_{θ_x,m_x} and C_{θ_y,m_y}, on the angle δ is shown in Fig. 5.3, which highlights that $C_{\theta_x,m_x} = C_{\theta_y,m_y}$ when $\delta = 90°$.

Results concerning this particular geometry (namely $\delta = 90°$) are then validated through FEA performed with the commercial software COMSOL. FEA simulations are executed by individually loading the chain along the axes x_0, y_0 and z_0. The compliance elements are simply computed as the ratios between each load component and the corresponding deformations. Table 5.2 compares the results obtained via analytical model and FEA. The comparison shows a close agreement be-

Table 5.2: Compliance elements of the 2-SF spherical chain and comparison between analytical and FEA results

Compliance elements	C_{x,f_x}	$C_{x,f_y} = C_{y,f_x}$	$C_{x,m_z} = C_{\theta_z,f_x}$	C_{y,f_y}	$C_{y,m_z} = C_{\theta_z,f_y}$	C_{z,f_z}
Analytic	7.3603e-4	-5.9730e-20	0.0127	7.3603e-4	-0.0127	0.0039
FEA	7.3631e-4	-5.9000e-20	0.0127	7.3635e-4	-0.0127	0.0038
Percentage error	0.038	1.22	0	0.038	0	2.56
Compliance elements	C_{θ_x,m_x}	$C_{z,m_x} = C_{\theta_x,f_z}$	$C_{z,m_y} = C_{\theta_y,f_z}$	C_{θ_y,m_y}	$C_{\theta_x,m_y} = C_{\theta_y,m_x}$	C_{θ_z,m_z}
Analytic	26.5379	-0.0334	0.0334	26.5379	-4.9013e-15	0.4827
FEA	26.5455	-0.0334	0.0334	26.5455	-4.9000e-15	0.4842
Percentage error	0.028	0	0	0.028	0.026	0.31

Table 5.3: Compliance elements of the 2-SBF spherical chain

Compliance elements	C_{x,f_x}	$C_{x,f_y} = C_{y,f_x}$	$C_{x,m_z} = C_{\theta_z,f_x}$	C_{y,f_y}	$C_{y,m_z} = C_{\theta_z,f_y}$	C_{z,f_z}
Value	8.0311e-4	-4.0926e-20	0.0133	8.0311e-4	-0.0133	0.0183

Compliance elements	C_{θ_x,m_x}	$C_{z,m_x} = C_{\theta_x,f_z}$	$C_{x,m_y} = C_{\theta_y,f_z}$	C_{θ_y,m_y}	$C_{\theta_x,m_y} = C_{\theta_y,m_x}$	C_{θ_z,m_z}
Value	26.5379	-0.0350	0.0350	26.5379	-1.5472e-15	0.4827

tween the two methods.

As a further step, an SF-based chain has been compared with a similar chain featuring SBF flexures and equal values of the principal compliance elements. Defining w and l as the SBF width and length, the latter design constraint is achieved whenever both SBFs and SFs are characterized by equal width (i.e. $w = r_o - r_i$), and same centroidal axes length (i.e. $l = R\theta$). By applying the method described in Section 5.2, the compliance matrix of the SBF-based chain has been computed and numerical data are shown in Table 5.3. The pictures of the two considered design solutions are reported in Figs. 5.4 and 5.5 which also show the chain deformed shapes (contour plot of the total displacement) when a generic torque lying in $x_0 - y_0$ plane is applied to the end-link.

The quantitative comparison between the two design solutions is then performed by defining three compliance ratios as follows:

$$r_1 = \frac{|C^{SF}_{x,f_x}|}{|C^{SBF}_{x,f_x}|}; \quad r_2 = \frac{|C^{SF}_{x,m_z}|}{|C^{SBF}_{x,m_z}|} = \frac{|C^{SF}_{\theta_z,f_x}|}{|C^{SBF}_{\theta_z,f_x}|} = \frac{|C^{SF}_{z,m_x}|}{|C^{SBF}_{z,m_x}|} = \frac{|C^{SF}_{\theta_x,f_z}|}{|C^{SBF}_{\theta_x,f_z}|}; \quad r_3 = \frac{|C^{SF}_{z,f_z}|}{|C^{SBF}_{z,f_z}|}; \qquad (5.8)$$

where each compliance element concerning the SF-based chain (referred to with SF superscript) is divided by the corresponding compliance element concerning the SBF-based chain (referred to with SBF superscript). In particular, the variables r_1, r_2, and r_3 represent ratios between undesired (secondary) compliances in all those applications requiring a spherical motion. Therefore, compliance ratios whose value is less than unity simply indicates that the SF-based chain out-
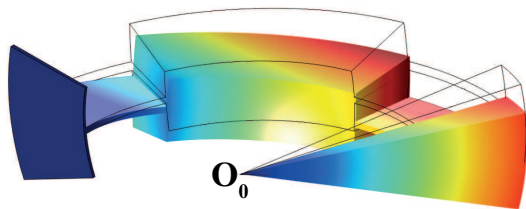
Figure 5.4: Finite element model of the 2-SF chain.
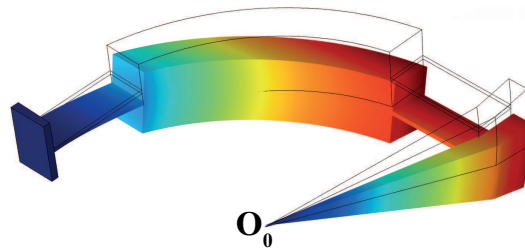
Figure 5.5: Finite element model of the 2-SBF chain.
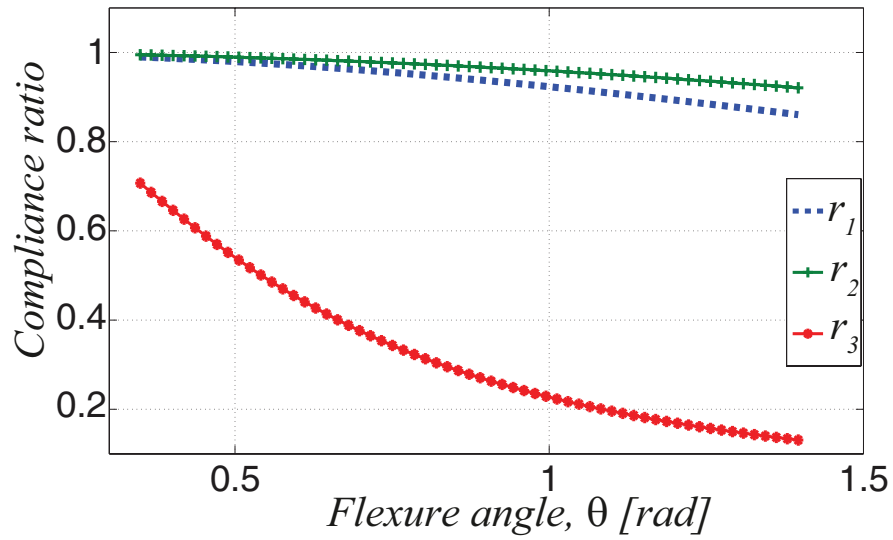
Figure 5.6: Influence of varying θ on compliance ratios

performs the SBF-based chain in terms of parasitic motions. As an example, for a given radius $R = 55.2mm$, the values of r_1, r_2 and r_3 as a function of θ are reported in Fig. 5.6. For a given angle $\theta = \pi/3$, the compliance ratios are constant (independent of R), namely $r_1 = 0.9191$, $r_2 = 0.9549$ and $r_3 = 0.2115$. In conclusion, for what concerns this particular case study, numerical simulations confirm the benefits when using the primitive SF as compared to the traditional SBF.

Chapter 6

Design and Analysis of a Fully Compliant Passive Spherical Joint Using Spherical Flexure Hinges

In this chapter, a new type of passive compliant spherical joint is represented. The joint is made by the in-parallel connection of two fully compliant spherical chains. Each chain is composed of three identical spherical flexures connected in-series with mutually orthogonal axes. The closed-form compliance equations for the spherical joint are derived via the previously described analytical method. The compliant spherical chain is also evaluated comparing with the equivalent compliant chain employing straight beam flexures.

6.1 Introduction

In previous chapter, relevant studies dedicated to compliant mechanisms involving spherical motions as well as compliant spherical mechanisms were reviewed and a fully compliant spherical chain with two degrees of freedom was introduced and evaluated. In this chapter, a compliant passive spherical joint is represented. Few studies have been dedicated to analysing and designing compliant passive spherical joints. Lobontiu and Paine [33] provided analytical solution for designing circular cross-section corner-filleted flexures (Fig. 6.1(a)) for three-dimensional compliant mechanisms. These flexures have been used as a compliant substitute for spherical pairs in the literature. However, they suffer from anisotropic deforming behavior unlike identical ball joints, and difficult machining and manufacturing process. Daihong et al. [50] have proposed a
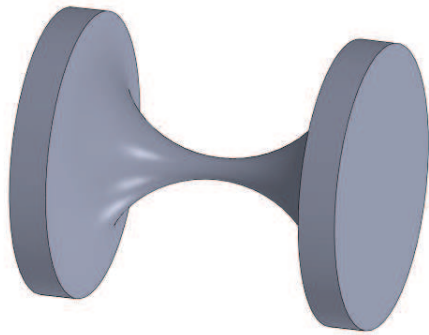
(a) Circular cross-section corner-filleted flexures
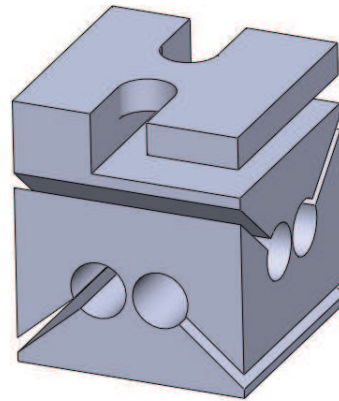
(b) Spherical joint proposed by Daihong et al. [50]
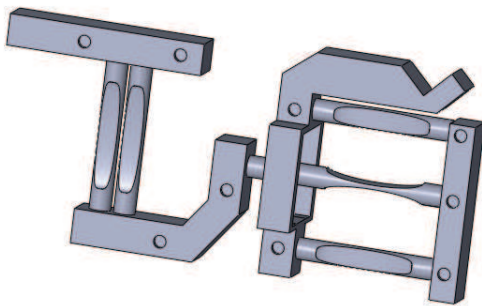
(c) Spherical joint proposed by Hesselbach et al. [44]
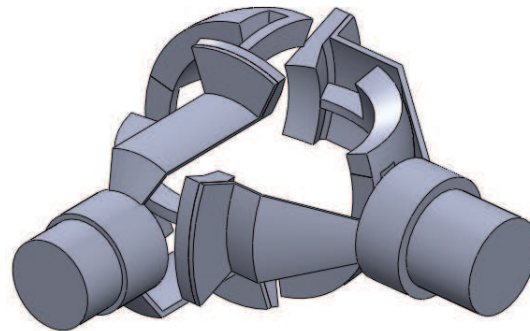
(d) Spherical joint presented in this study

Figure 6.1: Compliant spherical joints

cubic compliant spherical joint (Fig. 6.1(b)) to use in their 6-DOF compliant manipulator. They have used three circular flexures as revolute pairs with intersecting compliant axes. Hesselbach et al. [44] have applied three set of elliptical flexures in their composed compliant spherical joint (Fig. 6.1(c)). The spherical joint introduced in this chapter, is proposed using six identical SFs composing the in-parallel connection of two 3-SF compliant spherical chains (Fig. 6.1(d)). This joint demonstrates a fully isotropic and decoupled deformation behavior to applied loads.

6.2 Closed-Form Compliance Equations for the Spherical Joint

The compliant spherical pair proposed in this chapter is composed of two 3-SF compliant spherical chains and can provide 3 rotational degrees of freedom between the input shaft (fixed) and the output shaft as depicted in Fig. 6.2(a). Let us denote as Chain#1 (Fig. 6.2(b)) and Chain#2 (Fig.

(a) Compliant spherical joint studied in this chapter
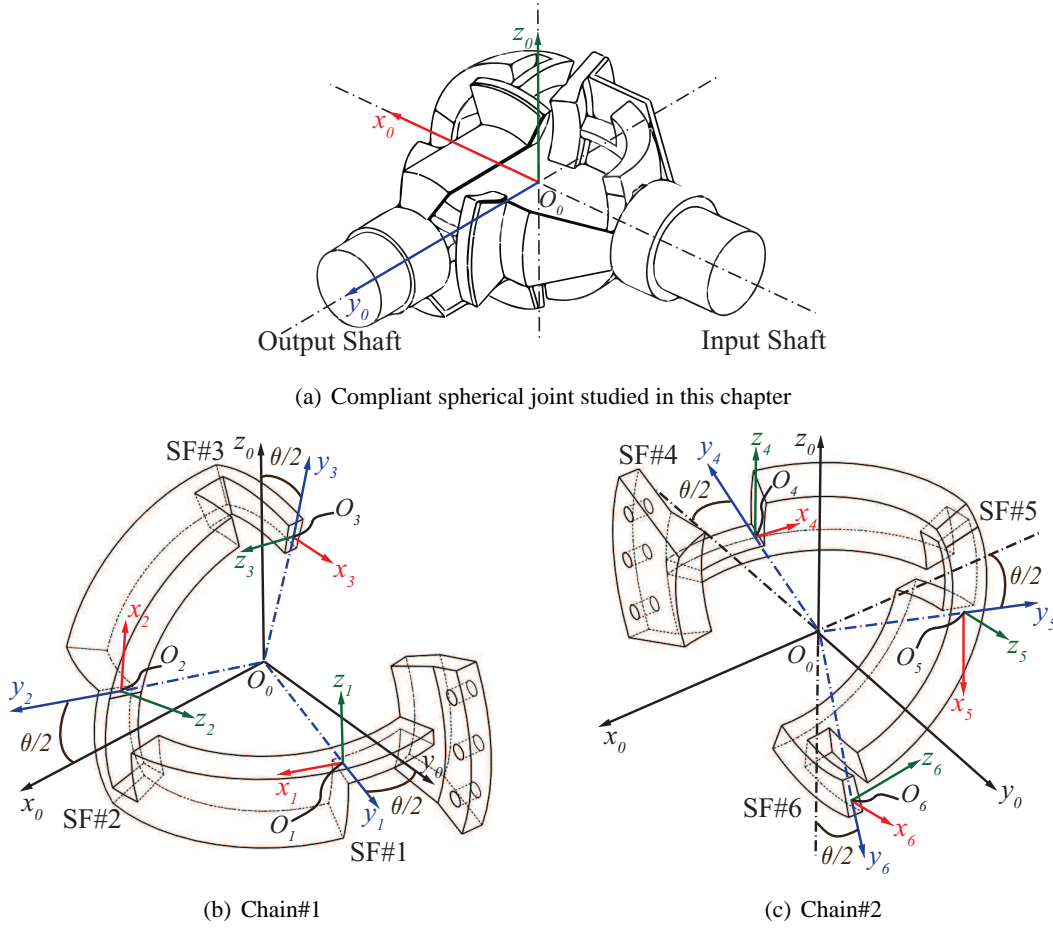
(b) Chain#1

(c) Chain#2

Figure 6.2: Compliant spherical joint composed of two spherical chains

6.2(c)), the upper and lower spherical chains respectively. Each chain is made by the in-series connection of three SFs (namely SF#1, 2, 3 for Chain#1 and SF#4, 5, 6 for Chain#2) as shown in Fig. 6.2. All of the SFs are identical to the SF represented in Chapter 4 (Fig. 4.1). The flexures in each chain are located such that their centriodal axes are lying in three mutually orthogonal planes. This imposes the joint to have an isotropic configuration. The frame S_0 is adopted at the center of the spherical motion (O_0) such that y_0, x_0 and z_0 axes pass through the geometric center of SF#1, 4, SF#2, 5 and SF#3, 6 respectively. Resorting to Eq. 5.3, the overall compliance matrix for Chain#1 and Chain#2 can be obtained as follows:

$$^0\mathbf{C}_{\text{Chain#1}} = \sum_{g=1}^{3} {}^0\mathbf{T}_g^{-T} \cdot {}^g\mathbf{C} \cdot {}^0\mathbf{T}_g^{-1} = \sum_{g=1}^{3} {}^g\mathbf{T}_0^T \cdot {}^g\mathbf{C} \cdot {}^g\mathbf{T}_0 \tag{6.1}$$

$$^0\mathbf{C}_{\text{Chain#2}} = \sum_{g=4}^{6} {}^0\mathbf{T}_g^{-T} \cdot {}^g\mathbf{C} \cdot {}^0\mathbf{T}_g^{-1} = \sum_{g=4}^{6} {}^g\mathbf{T}_0^T \cdot {}^i\mathbf{C} \cdot {}^g\mathbf{T}_0 \tag{6.2}$$

where $^g\mathbf{C}, g = 1...6$ is the compliance matrix of the SFs as obtained in Section 4.2 about their global coordinate frames. The adjoint matrix $^g\mathbf{T}_0$ relating $^g\mathbf{C}$ to S_0 can be determined using the proper rotation matrix ($^g\mathbf{R}_0$) and the translation vector ($^g\mathbf{r}_0$), recalling Eq. 5.1. In particular, $^g\mathbf{R}_0$ and $^g\mathbf{r}_0$ for the SFs are defined as follows:

$$^1\mathbf{R}_0 = \begin{bmatrix} \cos(\theta/2) & -\sin(\theta/2) & 0 \\ \sin(\theta/2) & \cos(\theta/2) & 0 \\ 0 & 0 & 1 \end{bmatrix}; \quad ^2\mathbf{R}_0 = \begin{bmatrix} 0 & -\cos(\theta/2) & -\sin(\theta/2) \\ 0 & \sin(\theta/2) & \cos(\theta/2) \\ 1 & 0 & 0 \end{bmatrix}; \quad (6.3)$$

$$^3\mathbf{R}_0 = \begin{bmatrix} -\sin(\theta/2) & 0 & \cos(\theta/2) \\ \cos(\theta/2) & 0 & \sin(\theta/2) \\ 0 & 1 & 0 \end{bmatrix}; \quad ^4\mathbf{R}_0 = \begin{bmatrix} -\cos(\theta/2) & \sin(\theta/2) & 0 \\ -\sin(\theta/2) & -\cos(\theta/2) & 0 \\ 0 & 0 & 1 \end{bmatrix};$$

$$^5\mathbf{R}_0 = \begin{bmatrix} 0 & \cos(\theta/2) & \sin(\theta/2) \\ 0 & -\sin(\theta/2) & -\cos(\theta/2) \\ 1 & 0 & 0 \end{bmatrix}; \quad ^6\mathbf{R}_0 = \begin{bmatrix} \sin(\theta/2) & 0 & -\cos(\theta/2) \\ -\cos(\theta/2) & 0 & -\sin(\theta/2) \\ 0 & 1 & 0 \end{bmatrix}$$

$$^1\mathbf{r_0} = {}^2\mathbf{r_0} = {}^3\mathbf{r_0} = {}^4\mathbf{r_0} = {}^5\mathbf{r_0} = {}^6\mathbf{r_0} = \begin{bmatrix} 0, & -R, & 0 \end{bmatrix}^T \quad (6.4)$$

where R and θ represent the radius and subtended angle of the SFs centroidal axes. By replacing Eqs. 6.3 and 6.4 to Eqs. 6.1 and 6.2 and recalling $^g\mathbf{C}$ from Table 4.1, the compliance matrices for the two spherical chains can be determined as follows:

$$^0\mathbf{C}_{\text{Chain\#1}} = \begin{bmatrix} C_{x,f_x} & 0 & 0 & 0 & C_{x,m_y} & C_{x,m_z} \\ 0 & C_{y,f_y} & 0 & C_{y,m_x} & 0 & C_{y,m_z} \\ 0 & 0 & C_{z,f_z} & C_{z,m_x} & C_{z,m_y} & 0 \\ 0 & C_{\theta_x,f_y} & C_{\theta_x,f_z} & C_{\theta_x,m_x} & 0 & 0 \\ C_{\theta_y,f_x} & 0 & C_{\theta_y,f_z} & 0 & C_{\theta_y,m_y} & 0 \\ C_{\theta_z,f_x} & C_{\theta_z,f_y} & 0 & 0 & 0 & C_{\theta_z,m_z} \end{bmatrix}_{\text{Chain\#1}} \quad (6.5)$$

$$^0\mathbf{C}_{\text{Chain\#2}} = \begin{bmatrix} C_{x,f_x} & 0 & 0 & 0 & C_{x,m_y} & C_{x,m_z} \\ 0 & C_{y,f_y} & 0 & C_{y,m_x} & 0 & C_{y,m_z} \\ 0 & 0 & C_{z,f_z} & C_{z,m_x} & C_{z,m_y} & 0 \\ 0 & C_{\theta_x,f_y} & C_{\theta_x,f_z} & C_{\theta_x,m_x} & 0 & 0 \\ C_{\theta_y,f_x} & 0 & C_{\theta_y,f_z} & 0 & C_{\theta_y,m_y} & 0 \\ C_{\theta_z,f_x} & C_{\theta_z,f_y} & 0 & 0 & 0 & C_{\theta_z,m_z} \end{bmatrix}_{\text{Chain\#2}} \quad (6.6)$$

Table 6.1: Compliance factors for the two spherical chains

$\{C_{x,f_x} = C_{y,f_y} = C_{z,f_z}\}_{\text{Chain\#1}} = \{C_{x,f_x} = C_{y,f_y} = C_{z,f_z}\}_{\text{Chain\#2}} = \dfrac{R\theta\left(I_nGJ+GJR^2A+R^2EAI_n\right)}{EAI_nGJ}$
$\{C_{x,m_y} = C_{y,m_z} = C_{z,m_x} = C_{\theta_x,f_z} = C_{\theta_y,f_x} = C_{\theta_z,f_y}\}_{\text{Chain\#1}} =$ $-\{C_{x,m_y} = C_{y,m_z} = C_{z,m_x} = C_{\theta_x,f_z} = C_{\theta_y,f_x} = C_{\theta_z,f_y}\}_{\text{Chain\#2}} = -2\dfrac{R^2\sin(\theta/2)}{GJ}$
$\{C_{\theta_x,m_x} = C_{\theta_y,m_y} = C_{\theta_z,m_z}\}_{\text{Chain\#1}} = \{C_{\theta_x,m_x} = C_{\theta_y,m_y} = C_{\theta_z,m_z}\}_{\text{Chain\#2}} = \dfrac{R\theta\left(I_nEI_m+I_nGJ+GJI_m\right)}{GJEI_mI_n}$
$\{C_{x,m_z} = C_{y,m_x} = C_{z,m_y} = C_{\theta_x,f_y} = C_{\theta_y,f_z} = C_{\theta_z,f_x}\}_{\text{Chain\#1}} =$ $-\{C_{x,m_z} = C_{y,m_x} = C_{z,m_y} = C_{\theta_x,f_y} = C_{\theta_y,f_z} = C_{\theta_z,f_x}\}_{\text{Chain\#2}} = 2\dfrac{R^2\sin(\theta/2)}{EI_n}$

The analytical expressions for the matrix entries are reported in Table 6.1. The cross section properties (A, I_m, I_n, and J) can be recalled from Section 4.3 as a function of the hinge geometric parameters.

A similar procedure can be adopted to obtain the overall compliance matrix of the spherical joint, considering the fact that for parallel combinations, stiffness matrices of the chains should be summed up in the same reference frame:

$$^0\mathbf{K} = \sum_{i=1}^{2} {}^0\mathbf{T}_i \cdot {}^i\mathbf{K} \cdot {}^0\mathbf{T}_i^T = {}^0\mathbf{C}_{\text{Chain\#1}}^{-1} + {}^0\mathbf{C}_{\text{Chain\#2}}^{-1} \tag{6.7}$$

The compliance matrix of the joint ($^0\mathbf{C}$), will be then obtained by inverting it's stiffness matrix:

$$^0\mathbf{C} = {}^0\mathbf{K}^{-1} \tag{6.8}$$

Matrix $^0\mathbf{C}$ relates the wrench $^0\mathbf{w}$ acting on S_0 to the corresponding generalized displacement $^0\mathbf{s}$ as follows:

$$^0\mathbf{s} = {}^0\mathbf{C} \cdot {}^0\mathbf{w} \tag{6.9}$$

$$^0\mathbf{s} = \begin{bmatrix} u_0 & v_0 & w_0 & \alpha_0 & \phi_0 & \psi_0 \end{bmatrix}^T$$

$$^0\mathbf{w} = \begin{bmatrix} f_{x_0} & f_{y_0} & f_{z_0} & m_{x_0} & m_{y_0} & m_{z_0} \end{bmatrix}^T$$

6.3 Numerical Example and Model Validation

The spherical joint depicted in Fig. 6.2 is considered for the case study. The joint is composed of two serial chains with six identical SFs. The SF geometric parameters and the material employed for the simulations are identical to the corresponding data used in Section 4.5. The analytical method described earlier and FEA are both used to evaluate the compliance matrices of Chain#1

Table 6.2: Compliance elements for Chain#1 and comparison between analytical and FEA results

Compliance elements	$C_{x,f_x} = C_{y,f_y} = C_{z,f_z}$	$C_{x,m_y} = C_{y,m_z} = C_{z,m_x} = C_{\theta_x,f_z} = C_{\theta_y,f_x} = C_{\theta_z,f_y}$
Analytic	0.0027	-0.0334
FEA	0.0027	-0.0335
Percentage error	0	0.3
Compliance elements	$C_{\theta_x,m_x} = C_{\theta_y,m_y} = C_{\theta_z,m_z}$	$C_{x,m_z} = C_{y,m_x} = C_{z,m_y} = C_{\theta_x,f_y} = C_{\theta_y,f_z} = C_{\theta_z,f_x}$
Analytic	26.7793	0.0127
FEA	26.7921	0.0129
Percentage error	4.77	1.55

Table 6.3: Compliance elements for Chain#2 and comparison between analytical and FEA results

Compliance elements	$C_{x,f_x} = C_{y,f_y} = C_{z,f_z}$	$C_{x,m_y} = C_{y,m_z} = C_{z,m_x} = C_{\theta_x,f_z} = C_{\theta_y,f_x} = C_{\theta_z,f_y}$
Analytic	0.0027	0.0334
FEA	0.0027	0.0335
Percentage error	0	0.3
Compliance elements	$C_{\theta_x,m_x} = C_{\theta_y,m_y} = C_{\theta_z,m_z}$	$C_{x,m_z} = C_{y,m_x} = C_{z,m_y} = C_{\theta_x,f_y} = C_{\theta_y,f_z} = C_{\theta_z,f_x}$
Analytic	26.7793	-0.0127
FEA	26.7921	-0.0129
Percentage error	4.77	1.55

and Chain#2. Table 6.2 and Table 5.3 compares the results obtained via analytical model and FEA for Chain#1 and Chain#2 respectively. One can notice the close agreement between the two methods from the comparison and the percentage error provided.

Following Eqs. 6.7 and 6.8, the overall compliance matrix for the joint and the relation between deformations and the loads acting at S_0 can be determined as follows:

$$
\begin{bmatrix} u_0 \\ v_0 \\ w_0 \\ \hline \alpha_0 \\ \phi_0 \\ \psi_0 \end{bmatrix} = \begin{bmatrix} 0.0013 & 7.9333e-6 & 7.9333e-6 & 0 & 0 & 0 \\ 7.9333e-6 & 0.0013 & 7.9333e-6 & 0 & 0 & 0 \\ 7.9333e-6 & 7.9333e-6 & 0.0013 & 0 & 0 & 0 \\ \hline 0 & 0 & 0 & 13.1498 & 0.0797 & 0.0797 \\ 0 & 0 & 0 & 0.0797 & 13.1498 & 0.0797 \\ 0 & 0 & 0 & 0.0797 & 0.0797 & 13.1498 \end{bmatrix} \cdot \begin{bmatrix} f_{x_0} \\ f_{y_0} \\ f_{z_0} \\ \hline m_{x_0} \\ m_{y_0} \\ m_{z_0} \end{bmatrix} \quad (6.10)
$$

As we can see from Eq. 6.10, the compliance matrix of the joint represents a fully isotopic be-

havior to applied loads and moments which is an ideal characteristic for spherical joints specially in compliant mechanisms and micro-manipulators. Furthermore, it comprises a unique property for this purpose specially encompassing decoupled deformation behavior to applied forces and moments. This indicates that if the joint is loaded purely with moments, the deformation profile of the joint will only comprise rotations exempt from undesired displacements.

In order to better understand the characteristics and competencies of SFs over commonly used flexures e.g. SBFs, the SF-based Chain#1 (SF-Chain) has been compared with a similar chain featuring SBFs (SBF-Chain). The SBF-Chain is composed of three identical SBFs such that the middle cross section centriod of the SBFs are located in a distance equal to R from the center of the spherical motion (O_0). Assuming the same conditions and following the same procedure depicted in section 6.2, the compliance matrix for the SBF-Chain is obtained as Eq. 6.5 with the following compliance elements:

$$C_{x,f_x} = C_{y,f_y} = C_{z,f_z} = \frac{l\left(w^2 + 12R^2\right)}{Etw^3} + \frac{l^3}{Etw^3} + \frac{l\left(l^2Gw^2 + l^2Gt^2 + 12R^2Et^2\right)}{Ewt^3G\left(w^2 + t^2\right)} \qquad (6.11)$$

$$C_{x,m_y} = C_{y,m_z} = C_{z,m_x} = C_{\theta_x,f_z} = C_{\theta_y,f_x} = C_{\theta_z,f_y} = -12\frac{Rl}{Gwt\left(w^2 + t^2\right)}$$

$$C_{\theta_x,m_x} = C_{\theta_y,m_y} = C_{\theta_z,m_z} = 12\frac{l}{Gwt\left(w^2 + t^2\right)} + 12\frac{l}{Ewt^3} + 12\frac{l}{Etw^3}$$

$$C_{x,m_z} = C_{y,m_x} = C_{z,m_y} = C_{\theta_x,f_y} = C_{\theta_y,f_z} = C_{\theta_z,f_x} = 12\frac{Rl}{Etw^3}$$

One can realize that there are 4 independent compliance elements and the structure of the matrix is similar to the SF-Chain. In order to compare these two chains, the SBF is characterized considering equal compliance factors for the two chains. This results in a system of 4 nonlinear equations. Since there are 3 unknowns for characterizing the SBF, the nonlinear system is solved assuming equal rotation-induced compliance factors and minimizing the $4th$ equation that involves pure displacements, to minimize the overall parasitic motions. Considering Eqs. 6.5 and 6.11, this system of equations can be simplified as:

$$\begin{cases} C_{x,m_y}^{(SF-Chain)} - C_{x,m_y}^{(SBF-Chain)} = 0 \\[2mm] C_{\theta_x,m_x}^{(SF-Chain)} - C_{\theta_x,m_x}^{(SBF-Chain)} = 0 \implies \text{Minimize}\left\{ C_{x,f_x}^{(SF-Chain)} - C_{x,f_x}^{(SBF-Chain)} \right\} \\[2mm] C_{x,m_z}^{(SF-Chain)} - C_{x,m_z}^{(SBF-Chain)} = 0 \end{cases}$$

This set of nonlinear equations is solved using numerical methods and the SBF is characterized as $l = 39.8\,mm$, $w = 9.3\,mm$ and $t = 0.87\,mm$. The compliance matrix entries for the SBF-Chain are defined as depicted in Table 6.4. By comparing the compliance elements represented for the two chains as reported in Table 6.2 and Table 6.4, one can notice that all the compliance elements

Table 6.4: Compliance elements for the SBF-Chain

Compliance elements	$C_{x,f_x} = C_{y,f_y} = C_{z,f_z}$	$C_{x,m_y} = C_{y,m_z} = C_{z,m_x} = C_{\theta_x,f_z} = C_{\theta_y,f_x} = C_{\theta_z,f_y}$
Value	0.0060	-0.0334

Compliance elements	$C_{\theta_x,m_x} = C_{\theta_y,m_y} = C_{\theta_z,m_z}$	$C_{x,m_z} = C_{y,m_x} = C_{z,m_y} = C_{\theta_x,f_y} = C_{\theta_y,f_z} = C_{\theta_z,f_x}$
Value	26.7793	0.0127

for the both chains are equal except the three for translational terms which are also representative of parasitic motions. This term is equal to 0.0027 for the SF-Chain and 0.006 for the SBF-Chain. This clarifies the outperforming behavior of SFs in comparison with SBFs in terms of parasitic motions. The numerical values of the compliance matrix entries for the SF-Chain and SBF-Chain are depicted in Fig. 6.3 and Fig. 6.4 respectively. As described in Section 3.4, this 3D bar graph representation allows a qualitative comparison of the spherical chains in terms of compliance factors.

As a further step, the SF and SBF have been compared in terms of maximum stress levels. Considering the von Mises criterion as explained in Section 4.4, the two flexures have been evaluated by the maximum von Mises stress when loaded with a unit (principal) bending moment m_y on the free end. In particular, the SBF assumes a constant value equaling $8.48e8\,Pa$ along its length where the stress distribution for the SF along its centroidal axis, is depicted in Fig. 6.5. The maximum stress for the SF occurs at its free end and is equal to $6.25e8\,Pa$. As we can see, the SF furthermore outperforms SBF in terms of maximum achievable rotation, being characterized by a lower stress level for equal load.
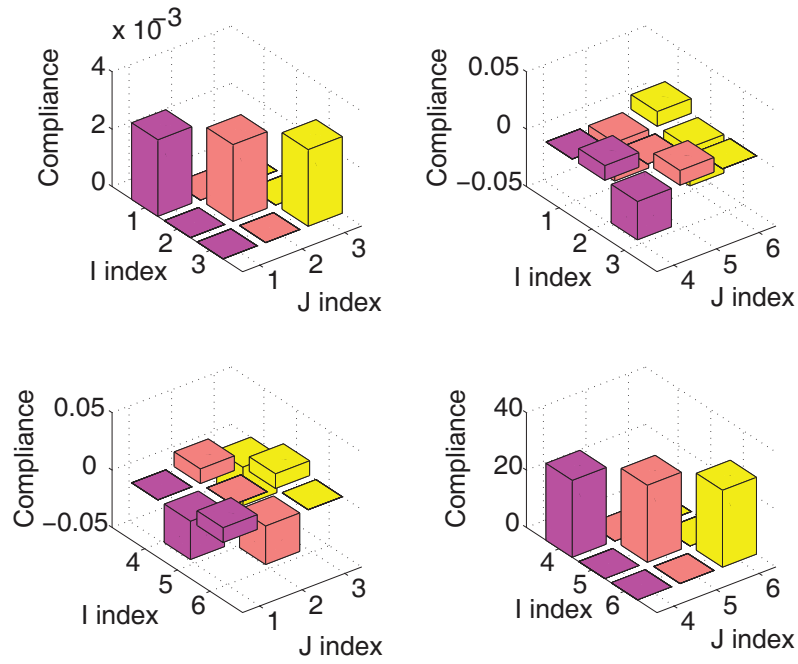
Figure 6.3: 3D bar representation for the SF-Chain compliance matrix
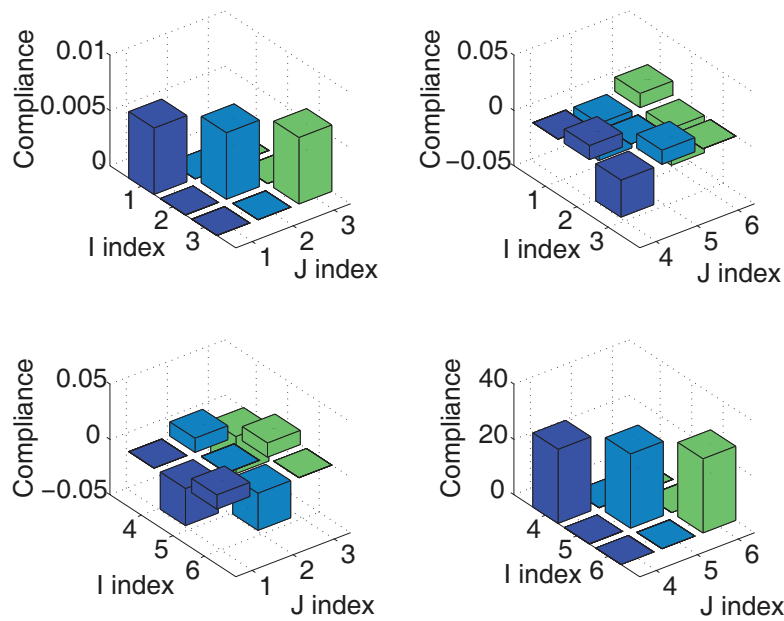
Figure 6.4: 3D bar representation for the SBF-Chain compliance matrix
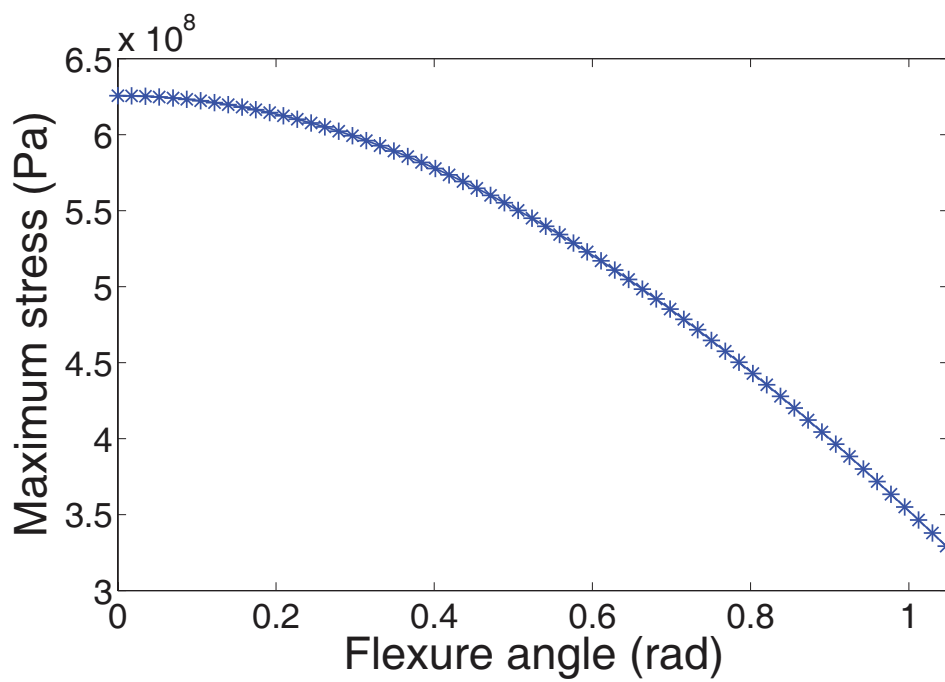
Figure 6.5: Maximum von Mises stress for the SF along its axis

Chapter 7

Conclusion

Flexure-based compliant mechanisms have become increasingly popular in different research areas, considering their advantages compared to traditional rigid-body mechanisms. These compliant mechanisms gain some or all of their mobility due to the elastic deformation of their flexible members known as flexure hinges. Flexure hinges are characterized by light weight, no need for lubrication, no backlash, no friction losses and an easy manufacturing process. In this thesis, new types of flexure hinges with curved centroidal axes were introduced and studied for both planar and spatial applications. First, circularly curved-beam flexures were characterized and particularly designed for planar applications, such as articulated robotic fingers. The closed-form compliance equations for this type of flexures were fully derived as a function of their geometric parameters and the employed material. These flexures were further compared to commonly used straight beam flexures considering the potential applications in the optimal design of compliant robotic fingers. It was shown that circularly curved-beam flexures are better alternatives for achieving maximum rotation demands in planar applications. Spherical flexure hinges were then introduced and specifically designed for spatial applications involving spherical motions such as compliant spherical mechanisms. These mechanisms are characterized by having all points of their links moving on concentric spherical surfaces, the center of these spheres being denoted as center of spherical motion. Spherical flexures were also characterized and their closed-form compliance equations were derived. Proposing a feasible framework for comparing these flexures with circularly curved-beam flexures, for what concerns their capability in providing spherical motions, proved that spherical flexures should be preferred over circularly curved-beam flexures when optimizing compliant spherical mechanisms. Spherical flexures were then used in compliant spherical chains and further evaluated comparing them with equivalent chains employing straight beam flexures. The comparison further highlighted the superior characteristics of spherical flexures. Finally a new passive compliant spherical joint was designed using spherical flexures. The overall compliance matrix of the joint demonstrated an exclusive deforming behavior with respect to applied loads.

Bibliography

[1] E. McEwen, R. L. Miller, C. A. Bergman, Early bow design and construction, Scientific American 264 (6) (1991) 76–82.

[2] W. Gurstelle, The Art of the Catapult: Build Greek Ballistae, Roman Onagers, English Trebuchets, and More Ancient Artillery, Chicago Review Press, 2004.

[3] Greek palintone, torsion-powered siege catapult, `http://antique.mrugala.net/Rome/Balliste%20romaine/Legion%20XXIV%20-%20roman%20ballista%20siege%20catapult.htm`, accessed: 2014-02-05.

[4] L. L. Howell, Compliant mechanisms, Wiley, New York, 2001.

[5] Y. Hirata, Liga process–micromachining technique using synchrotron radiation lithography–and some industrial applications, Nuclear Instruments and Methods in Physics Research Section B: Beam Interactions with Materials and Atoms 208 (2003) 21–26.

[6] F. Lotti, G. Vassura, A novel approach to mechanical design of articulated fingers for robotic hands, in: IEEE/RSJ International Conference on Intelligent Robots and Systems, Vol. 2, IEEE, 2002, pp. 1687–1692.

[7] N. Lobontiu, Compliant Mechanisms: Design of Flexure Hinges, CRC Press, 2002.

[8] A. Midha, I. Her, B. Salamon, Methodology for compliant mechanisms design: Part i- introduction and large-deflection analysis., in: 18 th Annual ASME Design Automation Conference, 1992, pp. 29–38.

[9] L. L. Howell, A. Midha, A method for the design of compliant mechanisms with small-length flexural pivots, Journal of Mechanical Design 116 (1) (1994) 280–290.

[10] L. Howell, A. Midha, Parametric deflection approximations for end-loaded, large-deflection beams in compliant mechanisms, Journal of Mechanical Design 117 (1) (1995) 156–165.

[11] J. R. Cannon, L. L. Howell, A compliant contact-aided revolute joint, Mechanism and machine theory 40 (11) (2005) 1273–1293.

[12] C. C. Tutum, et al., A compliant bistable mechanism design incorporating elastica buckling beam theory and pseudo-rigid-body model, Journal of Mechanical Design 130 (4) (2008) 042304.

[13] B. D. Jensen, L. L. Howell, D. B. Gunyan, L. G. Salmon, The design and analysis of compliant mems using the pseudo-rigid-body model, ASME-PUBLICATIONS-HTD 354 (1997) 119–126.

[14] S. Kota, Design of compliant mechanisms: applications to mems, in: 1999 Symposium on Smart Structures and Materials, International Society for Optics and Photonics, 1999, pp. 45–54.

[15] C. P. Lusk, L. L. Howell, Components, building blocks, and demonstrations of spherical mechanisms in microelectromechanical systems, Journal of Mechanical Design 130 (3) (2008) 034503.

[16] L. L. Howell, C. M. DiBiasio, M. A. Cullinan, R. M. Panas, M. L. Culpepper, A pseudo-rigid-body model for large deflections of fixed-clamped carbon nanotubes, Journal of Mechanisms and Robotics 2 (3) (2010) 034501.

[17] S. Zhang, E. D. Fasse, A finite-element-based method to determine the spatial stiffness properties of a notch hinge, ASME Journal of Mechanical Design 123 (1) (2001) 141–147.

[18] S. Timoshenko, J. Goodier, Theory of Elasticity, no. 3, McGraw Hill Higher Education, 1970.

[19] J. Paros, How to design flexure hinges, Mach Des 37 (1965) 151–156.

[20] B. Zettl, W. Szyszkowski, W. Zhang, On systematic errors of two-dimensional finite element modeling of right circular planar flexure hinges, Journal of mechanical design 127 (4) (2005) 782.

[21] W. Xu, T. King, Mechanical amplifier design for piezo-actuator applications, in: Innovative Actuators for Mechatronic Systems, IEE Colloquium on, IET, 1995, p. 1.

[22] N. Lobontiu, J. Paine, E. Garcia, M. Goldfarb, Corner-filleted flexure hinges, Journal of mechanical design 123 (3) (2001) 346–352.

[23] W. Schotborgh, F. Kokkeler, H. Tragter, F. van Houten, Dimensionless design graphs for flexure elements and a comparison between three flexure elements, Precision engineering 29 (1) (2005) 41–47.

[24] Y. Tian, B. Shirinzadeh, D. Zhang, Y. Zhong, Three flexure hinges for compliant mechanism designs based on dimensionless graph analysis, Precision Engineering 34 (1) (2010) 92–100.

[25] G. Chen, X. Liu, Y. Du, Elliptical-arc-fillet flexure hinges: Toward a generalized model for commonly used flexure hinges, Journal of mechanical design 133 (8) (2011) 81002.

[26] F. Lotti, G. Vassura, A novel approach to mechanical design of articulated fingers for robotic hands, in: IEEE/RSJ IROS International Conference on Intelligent Robots and Systems, 2002.

[27] G. Berselli, G. Vassura, M. Piccinini, Comparative evaluation of the selective compliance in elastic joints for robotic structures, IEEE ICRA, International Conference on Robotics and Automation (2011) 759–764.

[28] A. Dollar, R. Howe, A robust compliant grasper via shape deposition manufacturing, IEEE/ASME Transactions On Mechatronics 11 (2) (2006) 154–161.

[29] F. Parvari Rad, G. Berselli, R. Vertechy, V. Parenti-Castelli, Evaluating the spatial compliance of circularly curved-beam flexures, Springer, Computational Kinematics, Mechanisms and Machine Science Volume 15 (2014) 377–386.

[30] G. Berselli, F. Parvari Rad, R. Vertechy, V. Parenti-Castelli, Comparative evaluation of straight and curved beam flexures for selectively compliant mechanisms, in: IEEE/ASME International Conference on Advanced Intelligent Mechatronics (AIM), 2013, pp. 1761–1766.

[31] M. Jafari, M. Mahjoob, An exact three-dimensional beam element with nonuniform cross section, ASME Journal of Applied Mechanics 77 (6).

[32] N. Lobontiu, E. Garcia, Two-axis flexure hinges with axially-collocated and symmetric notches, Computers & Structures 81 (13) (2003) 1329–1341.

[33] N. Lobontiu, J. Paine, Design of circular cross-section corner-filleted flexure hinges for three-dimensional compliant mechanisms, Journal of mechanical design 124 (3) (2002) 479–484.

[34] S. Jagirdar, Kinematics of curved flexible beam, Ph.D. thesis, University of South Florida (2006).

[35] G. Li, G. Chen, Achieving compliant spherical linkage designs from compliant planar linkages based on prbm: A spherical young mechanism case study, in: Robotics and Biomimetics (ROBIO), 2012 IEEE International Conference on, IEEE, 2012, pp. 193–197.

[36] F. Parvari Rad, G. Berselli, R. Vertechy, V. Parenti-Castelli, Compliance based characterization of spherical flexure hinges for spatial compliant mechanisms, Springer, 19th CISM-IFToMM Symposium on Robot Design, Dynamics, and Control (In Press) (2014) 1–8.

[37] P. Burton, Kinematics and Dynamics of Planar Machinery, Prentice Hall, 1979.

[38] R. Huston, H. Josephs, Practical stress analysis in engineering design third edition, CRC Press, 2009.

[39] B. J. Wilson, J. F. Quereau, A simple method of determining stress in curved flexural members, University of Illinois, 1928.

[40] C. Chiang, Kinematics of Spherical Mechanisms, Krieger Publishing Company, 2000.

[41] S. Smith, Flexures, Elements of Elastic Mechanisms, Gordon and Breach Science Pub., 2000.

[42] B. Trease, Y. Moon, S. Kota, Design of large-displacement compliant joints, Journal of Mechanical Design 127 (4) (2005) 788–798.

[43] D. Farhadi Machekposhti, N. Tolou, J. L. Herder, The scope for a compliant homokinetic coupling based on review of compliant joints and rigid-body constant velocity universal joints, ASME IDETC, International Design Engineering Technical Conferences 4 (2012) 379–392.

[44] J. Hesselbach, J. Wrege, A. Raatz, O. Becker, Aspects on design of high precision parallel robots, Assembly Automation 24 (1) (2004) 49–57.

[45] G. Palmieri, M. C. Palpacelli, M. Callegari, Study of a fully compliant u-joint designed for minirobotics applications, ASME Journal of Mechanical Design 134 (11) (2012) 111003(9).

[46] J. O. Jacobsen, G. Chen, L. L. Howell, S. P. Magleby, Lamina emergent torsional (LET) joint, Mechanims and Machine Theory 44 (11) (2009) 2098–2109.

[47] M. Callegari, A. Cammarata, A. Gabrielli, M. Ruggiu, R. Sinatra, Analysis and design of a spherical micromechanism with flexure hinges, Journal of Mechanical Design 131 (2009) 051003.

[48] F. Parvari Rad, G. Berselli, R. Vertechy, V. Parenti-Castelli, Stiffness analysis of a fully compliant spherical chain with two degrees of freedom, Springer, Submitted to ARK, 14th International Symposium on Advances in Robot Kinematics (2014) 1–8.

[49] L. Carter Hale, Principles and techniques for designing precision machines, Ph.D. thesis, Dept. of Mech. Eng., MIT, Cambridge, MA (1999).

[50] C. Daihong, Z. Guanghua, L. Rong, Design of a 6-dof compliant manipulator based on serial-parallel architecture, in: IEEE/ASME International Conference on Advanced Intelligent Mechatronics, 2005, pp. 765–770.

Acknowledgements